REPORT DOCUMENTATION PAGE	Form Approved OMB NO. 0704-0188

1. REPORT DATE (DD-MM-YYYY) 16-09-2016	2. REPORT TYPE Final Report	3. DATES COVERED (From - To) 24-Jun-2013 - 23-Jun-2016

4. TITLE AND SUBTITLE	5a. CONTRACT NUMBER
Final Report: GeSn/Si Avalanche Photodetectors on Si substrates	W911NF-13-1-0196
	5b. GRANT NUMBER
	5c. PROGRAM ELEMENT NUMBER

6. AUTHORS	5d. PROJECT NUMBER
Shui-Qing (Fisher) Yu, Hameed Naseem	
	5e. TASK NUMBER
	5f. WORK UNIT NUMBER

7. PERFORMING ORGANIZATION NAMES AND ADDRESSES	8. PERFORMING ORGANIZATION REPORT NUMBER
University of Arkansas 210 Administration Building 1 University of Arkansas Fayetteville, AR 72701 -1201	

9. SPONSORING/MONITORING AGENCY NAME(S) AND ADDRESS (ES)	10. SPONSOR/MONITOR'S ACRONYM(S) ARO
U.S. Army Research Office P.O. Box 12211 Research Triangle Park, NC 27709-2211	11. SPONSOR/MONITOR'S REPORT NUMBER(S) 64461-EL-DRP.43

12. DISTRIBUTION AVAILIBILITY STATEMENT

Approved for Public Release; Distribution Unlimited

13. SUPPLEMENTARY NOTES
The views, opinions and/or findings contained in this report are those of the author(s) and should not contrued as an official Department of the Army position, policy or decision, unless so designated by other documentation.

14. ABSTRACT
In this project, firstly, the material growth of GeSn by chemical vapor deposition (CVD) system has been investigated. The material growth mechanism was in-depth studied; secondly, the material and optical characterizations have been conducted, including SEM, TEM, XRD, Raman, PL and ellipsometry spectroscopy. The results indicated that the device level material quality was achieved; thirdly, the GeSn samples were fabricated into LEDs and photo detectors, whose operating wavelength coverd from 1700 to 2600 nm. Particularly, the responsivity of GeSn photoconductor was higher than that of III-V photo detector, and the D* of GeSn photodiode

15. SUBJECT TERMS
GeSn,SiGeSn, CVD growth, mid-IR, photo detector

16. SECURITY CLASSIFICATION OF:			17. LIMITATION OF ABSTRACT	15. NUMBER OF PAGES	19a. NAME OF RESPONSIBLE PERSON Shui-Qing (Fisher) Yu
a. REPORT UU	b. ABSTRACT UU	c. THIS PAGE UU	UU		19b. TELEPHONE NUMBER 479-575-7265

Standard Form 298 (Rev 8/98)
Prescribed by ANSI Std. Z39.18

Report Title

Final Report: GeSn/Si Avalanche Photodetectors on Si substrates

ABSTRACT

In this project, firstly, the material growth of GeSn by chemical vapor deposition (CVD) system has been investigated. The material growth mechanism was in-depth studied; secondly, the material and optical characterizations have been conducted, including SEM, TEM, XRD, Raman, PL and ellipsometry spectroscopy. The results indicated that the device level material quality was achieved; thirdly, the GeSn samples were fabricated into LEDs and photo detectors, whose operating wavelength coverd from 1700 to 2600 nm. Particularly, the responsivity of GeSn photoconductor was higher than that of III-V photo detector, and the D* of GeSn photodiode was only one order of magnitude lower than that of extend-InGaAs detector, indicating the promising future applications of these type of photodetectors. Based on the characterization results, the GeSn photo detector as a potential candidate for low-cost uncooled multi-color infrared focal-plane-array was proposed.(FPA) application

Enter List of papers submitted or published that acknowledge ARO support from the start of the project to the date of this printing. List the papers, including journal references, in the following categories:

(a) Papers published in peer-reviewed journals (N/A for none)

Received	Paper
08/14/2014 1.00	Wei Du, Yiyin Zhou, Seyed A. Ghetmiri, Aboozar Mosleh, Benjamin R. Conley, Amjad Nazzal, Richard A. Soref, Greg Sun, John Tolle, Joe Margetis, Hameed A. Naseem, Shui-Qing Yu. Room-temperature electroluminescence from Ge/Ge1-xSnx/Ge diodes on Si substrates, Applied Physics Letters, (06 2014): 241110. doi: 10.1063/1.4884380
08/14/2014 2.00	Benjamin R. Conley, Aboozar Mosleh, Seyed Amir Ghetmiri, Wei Du, Richard A. Soref, Greg Sun, Joe Margetis, John Tolle, Hameed A. Naseem, Shui-Qing Yu. Temperature dependent spectral response and detectivity of GeSn photoconductors on silicon for short wave infrared detection, Optics Express, (06 2014): 15639. doi: 10.1364/OE.22.015639
TOTAL:	**2**

Number of Papers published in peer-reviewed journals:

(b) Papers published in non-peer-reviewed journals (N/A for none)

Received	Paper
TOTAL:	

Number of Papers published in non peer-reviewed journals:

(c) Presentations

Non Peer-Reviewed Conference Proceeding publications (other than abstracts):

Received   Paper

08/14/2014 5.00 Wei Du, Seyed Amir Ghetmiri, Aboozar Mosleh, Benjamin R. Conley, Liang Huang, Amjad Nazzal, Richard A Soref, Greg Sun, John Tolle, Hameed A. Naseem, Shuiqing Yu. Investigation of Photoluminescence from Ge1-xSnx: ACMOS-Compatible Material Grown on Si via CVDWei, the Conference On Lasers and Electrooptics. 08-JUN-14, . : ,

08/14/2014 6.00 Benjamin R. Conley, Liang Huang, Sayed Amir Ghetmiri, Aboozar Mosleh, Wei Du, Greg Sun, Richard Soref, John Tolle, Hameed A. Naseem, Shui-Qing Yu. Extended Infrared Absorption to 2.2 ?m with Ge1-xSnx Photodetectors Grown on Silicon, the Conference On Lasers and Electrooptics . 08-JUN-14, . : ,

08/14/2014 8.00 Seyed Amir Ghetmiri, Benjamin R. Conley, Aboozar Mosleh, Liang Huang, Wei Du, Amjad Nazzal, Greg Sun, Richard Soref, John Tolle, Hameed A. Naseem, Shui-Qing Yu. Photoluminescence from GeSn/Ge Heterostructure Microdisks with 6% Sn Grown on Si via CVD, the Conference On Lasers and Electrooptics . 08-JUN-14, . : ,

08/14/2014 9.00 Aboozar Mosleh, Seyed Amir Ghetmiri, Benjamin R. Conley, Wei Du, Hameed Naseem, Shui-Qing Yu, Richard A. Soref, Greg Sun, John Tolle, Joe Margetis. Strain Relaxation and Material Quality Improvement of Compressively Strained GeSn Epitaxial Films Through Cyclic Rapid Thermal Annealing Process, IEEE Summer Topicals Meeting Series 2014. 14-JUL-14, . : ,

08/14/2014 11.00 Benjamin R. Conley, Aboozar Mosleh, Seyed A. Ghetmiri, Wei Du, Hameed Naseem, Shui-Qing Yu, Richard A. Soref, Greg Sun, John Tolle, Joe Margetis. Temperature Dependent Spectral Response and Responsivity of GeSn Photoconductor on Si, IEEE Summer Topicals Meeting Series 2014. 14-JUL-14, . : ,

08/14/2014 14.00 B. R. Conley, A. Mosleh, S. A. Ghetmiri, W. Du, G. Sun, R. Soref, J. Margetis, J. Tolle, H. A. Naseem, S.-Q. Yu. Stability of pseudomorphic and compressively strained GeSn thin films under rapid thermal annealing, the 226th ECS Fall Meetings. 05-OCT-14, . : ,

08/14/2014 15.00 John Tolle, Joe Margetis, Seyed A. Ghetmiri, Aboozar Mosleh, Benjamin R. Conley, Wei Du, Amjad Nazzal, Richard A. Soref, Greg Sun, Hameed A. Naseem, Shui-Qing Yu. Growth and characterization of Ge1-xSnx alloys deposited using a commercial CVD system, the 226th ECS Fall Meetings. 05-OCT-14, . : ,

08/14/2014 12.00 Wei Du, Seyed Amir Ghetmiri, Aboozar Mosleh, Benjamin R. Conley, Liang Huang, Amjad Nazzal, Richard A. Soref, Greg Sun, John Tolle, Joe Margetis, Hameed A. Naseem, Shui-Qing Yu. Direct transition Ge0.94Sn0.06 PIN-diode double heterostructure light emitter at high injection, the 11th International Conference on Group IV Photonics. 27-AUG-14, . : ,

08/14/2014 13.00 Benjamin R. Conley, Yiyin Zhou, Aboozar Mosleh, Seyed Amir Ghetmiri, Wei Du, Richard A Soref, Greg Sun, Joe Margetis, John Tolle, Hameed A. Naseem, Shui-Qing Yu. Infrared spectral response of a GeSn p-i-n photodiode on Si, the 11th International Conference on Group IV Photonics. 27-AUG-14, . : ,

08/14/2014 16.00 Yiyin Zhou, Wei Du, Seyed Amir Ghetmiri, Aboozar Mosleh, Amjad Nazzal, Richard A Soref, Greg Sun, Joe Margetis, John Tolle, Hameed A. Naseem, Shui-Qing Yu. Room-temperature electroluminescence from Ge/Ge0.92Sn0.08/Ge double heterostructure LED on Si, IEEE Photonics Conference. 12-OCT-14, . : ,

08/14/2014 17.00 Thach Pham, Benjamin R. Conley, Liang Huang, Wei Du, Richard A Soref, Greg Sun, Joe Margetis, John Tolle, Hameed A. Naseem, Shui-Qing Yu. Enhanced responsivity by integration of interdigitatedelectrodes on Ge0.93Sn0.07 infrared photodetectors,
IEEE Photonics Conference. 12-OCT-14, . : ,

09/16/2016 42.00 Thach, Pham; Wei, Du; Huong, Tran; Joe, Margetis; John, toll; Gregory, Sun; Richard, soref; Hameed, Naseem; Baohua, Li; Mansour, Mortazavi; and Shui-Qing, Yu. Systematic study of Si-based Ge/Ge_0.9Sn_0.1/Ge photodiodes with 2.6 μm detector cutoff,
CLEO: Science and Innovations. 16-SEP-16, San Jose, California. : ,

TOTAL: **12**

Number of Non Peer-Reviewed Conference Proceeding publications (other than abstracts):

Peer-Reviewed Conference Proceeding publications (other than abstracts):

<u>Received</u>   <u>Paper</u>

07/29/2015 26.00 Seyed Amir Ghetmiri, Wei Du, Yiyin Zhou, Joe Margetis, Thach Pham, Aboozar Mosleh, Benjamin Conley, Amjad Nazzal, Gregory Sun, Richard Soref, John Tolle, Hameed Naseem, Baohua Li, Shui-Qing Yu. Temperature-dependent Characterization of G_0.94Sn_0.06 Light-Emitting Diode Grown on Si via CVD,
CLEO: Applications and Technology. 10-MAY-15, San Jose, California. : ,

07/29/2015 25.00 Thach Pham, Benjamin Conley, Joe Margetis, Huong Tran, Seyed Amir Ghetmiri, Aboozar Mosleh, Wei Du, Gregory Sun, Richard Soref, John Tolle, Hameed Naseem, Baohua Li, Shui-Qing Yu. Enhanced Responsivity up to 2.85 A/W of Si-based Ge_0.9Sn_0.1 Photoconductors by Integration of Interdigitated Electrodes,
CLEO: Science and Innovations. 10-MAY-15, San Jose, California. : ,

07/29/2015 27.00 S. Q. Yu, S. A. Ghetmiri, W. Du, J. Margetis, Y. Zhou, A. Mosleh, S. Al-Kabi, A. Nazzal, G. Sun, R. A. Soref, J. Tolle, B. Li, H. A. Naseem. Si based GeSn light emitter: mid-infrared devices in Si photonics,
SPIE OPTO. 27-FEB-15, San Francisco, California, United States. : ,

07/29/2015 28.00 Thach Pham, Wei Du, Joe Margetis, Seyed A. Ghetmiri, Aboozar Mosleh, Greg Sun, Richard A. Soref, John Tolle, Hameed A. Naseem, Baohua Li, Shui-Qing Yu. Temperature-dependent study of Si-based GeSn photoconductors,
SPIE OPTO. 27-FEB-15, San Francisco, California, United States. : ,

07/29/2015 29.00 Thach Pham, Benjamin R. Conley, Liang Huang, Wei Du, Seyed Amir Ghetmiri, Aboozar Mosleh, Amjad Nazzal, Richard A. Soref, Greg Sun, Joe Margetis, John Tolle, Hameed A. Naseem, Shui-Qing Yu. Enhanced responsivity by integration of interdigitated electrodes on Ge0.93Sn0.07 infrared photodetectors,
2014 IEEE Photonics Conference (IPC). 11-OCT-14, San Diego, CA. : ,

07/29/2015 30.00 Yiyin Zhou, Wei Du, Seyed Amir Ghetmiri, Aboozar Mosleh, Amjad Nazzal, Richard A. Soref, Greg Sun, Joe Margetis, John Tolle, Hameed A. Naseem, Shui-Qing Yu. Room-temperature electroluminescence from Ge/Ge0.92Sn0.08/Ge double heterostructure LED on Si,
2014 IEEE Photonics Conference (IPC). 11-OCT-14, San Diego, CA. : ,

08/04/2015 31.00 Wei Du, Thach Pham, Joe Margetis, Huong Tran, Seyed A. Ghetmiri, Aboozar Mosleh, Greg Sun, Richard A. Soref, John Tolle, Hameed A. Naseem, Baohua Li, Shui-Qing Yu. Si based mid-infrared GeSn photo detectors and light emitters,
SPEI Optics+Photonics. 09-AUG-15, . : ,

08/04/2015 32.00 Aboozar Mosleh, Murtadha Alher, Wei Du, Larry C. Cousar, Seyed Amir Ghetmiri, Sattar Al-Kabi, Wei Dou, Perry C. Grant, Benjamin R. Conley, Greg Sun, Richard A. Soref, Baohua Li, Hameed A. Naseem, Shui-Qing Yu. Growth and characterization of buffer-free SiGeSn epitaxial layers on Si for photonic applications,
57th Electronic Materials Conference. 24-JUN-15, . : ,

08/04/2015 33.00 Wei Du, Huong Tran, Sattar Al-Kabi, Greg Sun, Richard Sorf, John Tolle, Joe Margetis, Baohua Li, Hameed A. Nasee, Shui-Qing Yu, Seyed Amir Ghetmiri. Material and Optical Characterizations for Both Bulk and NIP double Heterostructure of Germanium Tin,
57th Electronic Materials Conference. 24-JUN-15, . : ,

  TOTAL: **9**

Number of Peer-Reviewed Conference Proceeding publications (other than abstracts):

(d) Manuscripts

Received | Paper

08/14/2014 3.00 Seyed Amir Ghetmiri, Wei Du, Benjamin R. Conley, Aboozar Mosleh, Amjad Nazza, Richard A. Soref, Greg Sun, Joe Margetis, John Tolle, Hameed A. Naseem, Shui-Qing Yu. Near and mid-infrared photoluminescence from Ge1-xSnx thin films on silicon,
Semiconductor Science and Technology (04 2014)

08/14/2014 4.00 Wei Du, Seyed A. Ghetmiri, Benjamin R. Conley, Aboozar Mosleh, Amjad Nazzal, Richard A. Soref, Greg Sun, John Tolle, Joe Margetis, Hameed A. Naseem, Shui-Qing Yu. Competition of optical transitions between direct and indirect bandgaps in Ge1-xSnx,
Applied Physics Letters (07 2014)

   TOTAL: **2**

Number of Manuscripts:

Books

Received | Book

   TOTAL:

Received | Book Chapter

   TOTAL:

Patents Submitted

Patents Awarded

Awards

Graduate Students

NAME	PERCENT_SUPPORTED	Discipline
Huong Tran	0.50	
FTE Equivalent:	**0.50**	
Total Number:	**1**	

Names of Post Doctorates

NAME	PERCENT_SUPPORTED
FTE Equivalent:	
Total Number:	

Names of Faculty Supported

NAME	PERCENT_SUPPORTED	National Academy Member
Shui-Qing Yu	0.00	
Hameed Naseem	0.00	
FTE Equivalent:	**0.00**	
Total Number:	**2**	

Names of Under Graduate students supported

NAME	PERCENT_SUPPORTED
FTE Equivalent:	
Total Number:	

Student Metrics
This section only applies to graduating undergraduates supported by this agreement in this reporting period

The number of undergraduates funded by this agreement who graduated during this period: 0.00

The number of undergraduates funded by this agreement who graduated during this period with a degree in science, mathematics, engineering, or technology fields:...... 0.00

The number of undergraduates funded by your agreement who graduated during this period and will continue to pursue a graduate or Ph.D. degree in science, mathematics, engineering, or technology fields:...... 0.00

Number of graduating undergraduates who achieved a 3.5 GPA to 4.0 (4.0 max scale):...... 0.00

Number of graduating undergraduates funded by a DoD funded Center of Excellence grant for Education, Research and Engineering:...... 0.00

The number of undergraduates funded by your agreement who graduated during this period and intend to work for the Department of Defense 0.00

The number of undergraduates funded by your agreement who graduated during this period and will receive scholarships or fellowships for further studies in science, mathematics, engineering or technology fields: 0.00

Names of Personnel receiving masters degrees

NAME

Total Number:

Names of personnel receiving PHDs

NAME

Total Number:

Names of other research staff

NAME   PERCENT_SUPPORTED

FTE Equivalent:
Total Number:

Sub Contractors (DD882)

Inventions (DD882)

Scientific Progress

See Attachment.

Technology Transfer

N.A.

GeSn/Si Avalanche Photodetectors on Si substrates

Final Report Submitted to

Contract No: W911NF-13-1-0196

By

Dr. Shui-Qing (Fisher) Yu

Dr. Hameed Naseem

Department of Electrical Engineering

University of Arkansas, Fayetteville, AR

Final Technical Report

"GeSn/Si Avalanche Photodetectors on Si substrates"

Shui-Qing (Fisher) Yu, Hameed Naseem

University of Arkansas

Report Period: June 24, 2013 – June 23, 2016

Team Management: In this project, we have built the research team after the project awarded in year one and we have maintained the research team for the following two years. The major team members are listed below:

- **Postdoc research associate.** Dr. Wei Du, with 7 years of device fabrication and characterization experiences, worked on this project from July 2013 to August 2015; Dr. Aboozar Mosleh, with 6 years of material growth and characterization experiences, worked on this project as a postdoc associate after his graduation from Drs. Yu and Naseem's group in August 2015. Drs. Du and Mosleh were responsible for ensuring the delivery of the project as well as helping PI supervise the students.

- **Ph.D. students.** Four Ph.D. students were designated to work on this project. The research tasks of those students have been more specifically defined to properly match the project targets. A list of student names and their research directions in this project is given in below.

Name	Degree/Department	Research direction
Benjamin R. Conley*	Ph.D./ Microelectronics-Photonics	Design, modeling, fabrication and characterization of GeSn-based Avalanche Photodetector.
Huong Tran**	Ph.D./ Electrical Engineering	Design, modeling, and characterization of GeSn-based Avalanche Photodetector.
Thach Pham	Ph.D./ Electrical Engineering	Fabrication and characterization of GeSn-based photoconductor and photodetector.
Seyed A. Ghetmiri	Ph.D./ Microelectronics-Photonics	Characterization of GeSn-based photoconductor and photodetector.

* Graduated on December 2014.
** Moved to a different project on December 2015.

Table of Contents

List of Tables

State of the problem studied

The goal of this project is to investigate the feasibility of utilizing unique optical absorption properties of novel all group IV GeSn compounds to develop high performance near infrared photo detectors at telecom wavelength and also to seek for a path way toward the development of the third generation focal plane arrays in mid-IR wavelength range. The whole device structure will be grown by a unique home-built Ultra-high vacuum Chemical Vapor Deposition (UHV-CVD) machine. The detailed problems are itemized in below:

- **Novel CVD techniques for device quality GeSn growth**: A novel UHV-CVD machine has been constructed with a variety of innovative control mechanism for device quality GeSn growth. The growth mechanism was comprehensively investigated;

- **Material characterizations**: Variety of material characterization methods were used to study the material properties, including film thickness, Si and Sn compositions, strain status and defect density, which provided the feedback for material growth;

- **Optical characterization**: Raman, photoluminescence, and ellipsometry spectroscopy were used to study the optical properties, which provided key information for the design of GeSn-based optoelectronic device;

- **Development of GeSn photoconductors**: GeSn photoconductors were used as test vehicles to establish the baseline of using GeSn material for mid-IR photodetector applications. Thick GeSn layer was grown and novel device structure was fabricated to enhance the photoconductive gain so that the responsivity of GeSn photoconductor could compete with the market dominating III-V IR photodetectors;

- **Development of GeSn photodiode**: GeSn double heterostructure PIN photodiode was comprehensively studied. The spectral response cut off wavelength was beyond 2 μm. The spectral D* was only one order of magnitude lower than that of market dominating III-V IR photodetectors. The broad wavelength coverage and the CMOS compatible growth technique make the GeSn photodiodes potentially viable for the development of low-cost, uncooled, multi-color, infrared focal-plane-array detectors;

- **Preliminary study of GeSn avalanche photodiode (APD):** The GeSn APD with separate absorption-charge-multiplication (SACM) structure was grown and characterized. The design took advantage of the excellent optical absorption of GeSn at mid-IR range and the outstanding carrier multiplication properties of Si. The preliminary results showed clear breakdown behavior;

Summary of the most important results

A list of work performed in this project and highlights of results are given in below.

- Both $SnCl_4$ and SnD_4 as Sn precursors are used for GeSn and SiGeSn growth (The only team in the world demonstrated such growth capability for both precursors);

- No buffer layer needed during the GeSn growth (First demonstration in the world using these precursors);

- Growth of GeSn and SiGeSn has been demonstrated. The incorporation of Si and Sn in Ge has been identified;

- Detailed material characterization has been conducted, which provided the feedback (material quality, defect density, etc.) for the material growth;

- A direct bandgap $Ge_{0.9}Sn_{0.1}$ alloy has been experimentally identified (First demonstration of GeSn in the world);

- PL spectra of GeSn bulk samples with Sn composition up to 12% have been obtained at temperatures from 77 to 300 K. PL peaks of n-type doped GeSn samples have been investigated. Bandgap shrinkage has been observed in heavily doped n-type samples;

- The systematic study of the absorption coefficient and refractive index of GeSn thin films (Sn from 0 to 10%) were conducted via spectroscopic ellipsometry at room temperature;

- Temperature-dependent electroluminescence (EL) spectra of the GeSn LEDs with Sn compositions from 6 to 10% have been investigated. The red-shift of EL peak with higher Sn composition has been observed. The peak powers of 28 and 50 mW for a 10% Sn surface emitting LED and an 8% Sn edge emitting LED were obtained;

- Spectral photo response of photoconductors with Sn compositions up to 10% has been investigated with longwave cutoff extended to 2.4 µm;

- The responsivity of 1.63 A/W at 1.55 µm has been achieved with a $Ge_{0.9}Sn_{0.1}$ standard photoconductor at 77 K, which is higher than that of market dominating Ge (0.8 A/W) and standard InGaAs (1.05 A/W) detectors at the same wavelength; A newly designed photoconductor with interdigitated electrodes has been fabricated and characterized. Due to the reduced carrier transit time, a high gain is achieved. As a result, a measured responsivity of 2.85 A/W at 77 K has been obtained at 1.55 µm;

- Systematic studies of 7 and 10% Sn DHS photodiode detectors were conducted at temperatures ranging from 300 to 77 K. The electrical parameters were extracted from temperature dependent I-V characteristics. A spectral response cutoff wavelength of 2.6 µm was observed for the 10% Sn device at 300 K. The peak D* were calculated as 4×10^9 and 2.4×10^9 cmHz$^{0.5}$W^{-1} at 77 K for 7 and 10% Sn devices, respectively;

- A side by side comparison for D* between GeSn and other market dominating IR detectors in short-IR wavelength (First time reported the D* of a GeSn detector in the world). The D* of GeSn photodiode (10% Sn) showed only one order of magnitude lower than those of extended-InGaAs detectors.

Major research content

The major research in this project had been focused on three directions:

I) GeSn and SiGeSn material growth and characterization
II) Optical characterization of GeSn materials
III) Fabrication and characterization of GeSn-based optoelectronic devices

I) GeSn and SiGeSn material growth and characterization

GeSn growth using UHV-CVD system: The ultra-high vacuum chemical vapor deposition (UHV-CVD) system located at University of Arkansas is used to grow Ge and GeSn films. A brief summary of material growth using CVD methods by different research groups is shown in Table I, which also indicates the uniqueness of this work in University of Arkansas.

Table I A brief summary of material growth using CVD methods by different research groups

Growth team	Growth system	Ge precursor	Sn precursor	Carrier gas	Buffer layer	SiGeSn growth
Arizona State University	UHV-CVD	Different chemistries	SnD_4	H_2	No	Yes
ASM/UA	RP-CVD	GeH_4	$SnCl_4$	N_2/H_2	Ge	Yes
IMEC	AP-CVD	Ge_2H_6	$SnCl_4$	N_2/H_2	Ge	No
Applied Materials	RP-CVD	Ge_2H_6	$SnCl_4$	$Ar/N_2/H_2$	Ge	No
Peter Grünberg Institute	RP-CVD	Ge_2H_6	$SnCl_4$	Ar/H_2	No	Yes
Translucent	Hot wall UHV-CVD	GeH_4	SnD_4	N. A.	No	Yes
University of Arkansas	**Cold wall UHV-CVD**	**GeH_4**	**$SnCl_4/SnD_4$**	**No**	**No**	**Yes**

A brief summary of material growth for Ge, SiGe, SiSn, GeSn and SiGeSn is shown in Table II.

Table II A brief summary of material growth for Ge, SiGe, SiSn, GeSn, and SiGeSn

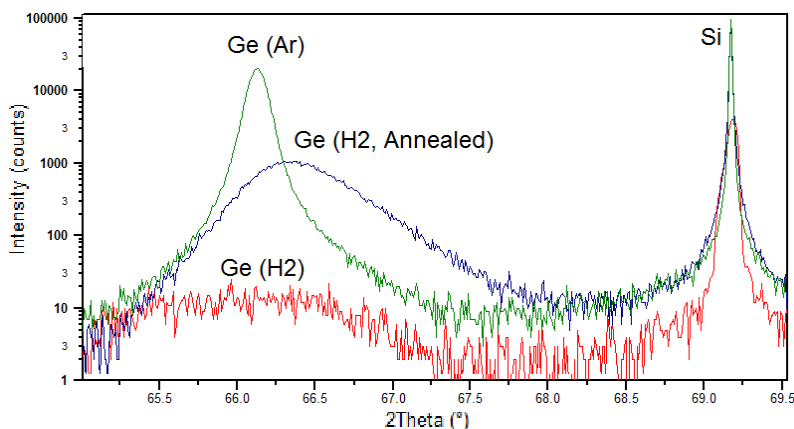| Epitaxy layer	Ge	SiGe	SiSn	GeSn		SiGeSn	
Precursors	GeH_4	SiH_4, GeH_4, Ar	SiH_4, $SnCl_4$	GeH_4		SiH_4, GeH_4	
Sn precursor				$SnCl_4$	SnD_4	$SnCl_4$	SnD_4
Total Number of round	126	44	10	127	39	27	22

Fig.1. 2Theta-Omega scan of the grown Ge films on Si. Germanium is at lower angle due to smaller lattice size.

The base pressure of this system reaches 10^{-10} torr, however, the growth pressure is ranged between 0.1 to 1 torr. In order to achieve high quality Ge layers a two-step method is adopted. Initial nucleation step is done at 300 ^{o}C and the growth is done at 550 ^{o}C. Using hydrogen carrier gas did not provide high quality Ge films. Although a post growth annealing of the film at 800 ^{o}C increases the quality of the film, using Ar as the carrier gas showed the highest quality. Figure 1 shows the X ray diffraction under these two conditions.
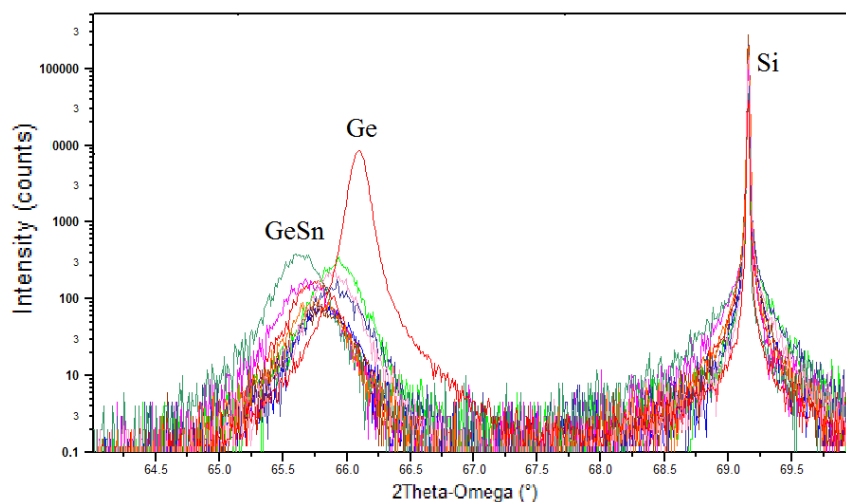
Fig. 2. 2Theta-Omega XRD scan of the grown GeSn layers. The GeSn peak can be seen on the lower angle in comparison with Ge due to higher lattice constant.

Growth of GeSn was the step after successful Ge growth. Incorporation of Sn into Ge is challenging due large lattice mismatch between Si, Ge and GeSn. Growth at high temperatures is not successful due to precipitation of Sn from Ge lattice. Thereupon, a temperature growth method is adopted. Growth of 2-3% Sn was successfully achieved by using UHV-CVD chamber. Figure 2 shows the XRD results for GeSn growth. It can be clearly seen that due to larger lattice size of GeSn the peak position is shifted to lower angles.
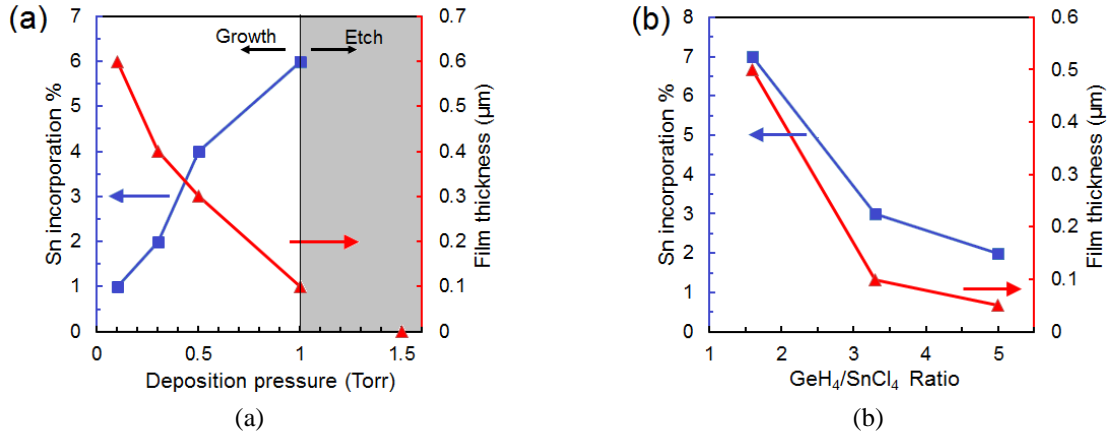
Fig. 3. (a) Sn incorporation percentage and film thickness as the functions of deposition pressure. The fixed gas flow ratio of GeH$_4$/SnCl$_4$=1.6. Films were etched off when pressure was higher than 1 Torr. (b) Sn incorporation percentage and film thickness as the functions of gas flow ratio. The fixed deposition pressure is 0.5 Torr.

The study of growth mechanism using SnCl$_4$ and GeH$_4$ as precursors for GeSn deposition has been conducted. Fig. 3(a) shows the GeSn thin films grown on Si at different pressures. Growth starts happening from 0.1 Torr and continues until the pressure reaches 1 Torr. When the pressure is higher than 1 Torr, the films are etched off. Fig. 3(b) shows GeSn growth results at different gas flow ratios of GeH$_4$/SnCl$_4$. The pressure is fixed at 0.5 Torr.
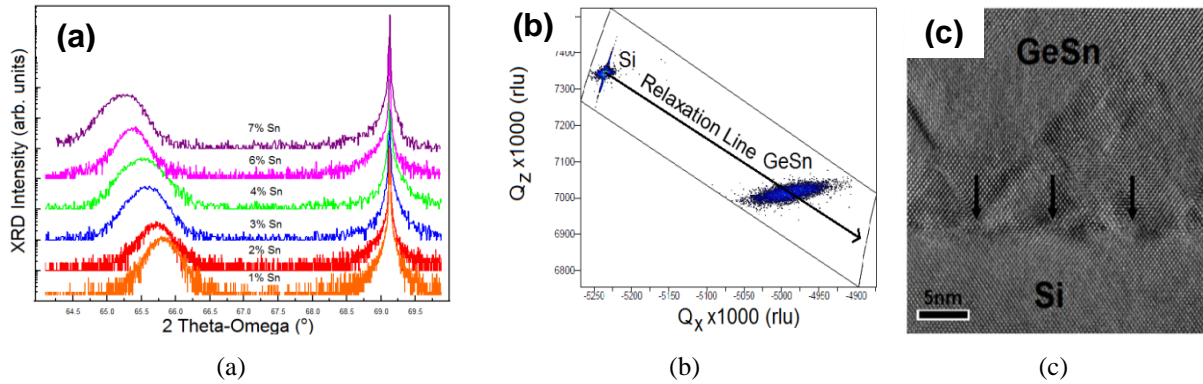
Fig. 4. (a) Symmetric (0 0 4) 2θ-ω scan of GeSn films. The peak at 69° is attributed to Si substrate and the peaks between 66-65° belong to GeSn films. (b) Reciprocal space map (RSM) from asymmetrical plane (-2 -2 4) for Ge$_{0.94}$Sn$_{0.06}$. The RSM shows that the film is strain relaxed on Si substrate. (c) TEM images of Ge$_{0.94}$Sn$_{0.06}$ film. The arrows show misfit dislocations formed at GeSn/Si interface due to the large lattice mismatch between Si and GeSn.

Material characterization results are summarized in Fig. 4. Analysis of Sn mole fraction, lattice constant, growth quality and strain in the GeSn films has been performed using high resolution X-ray diffraction (HRXRD) and high resolution transmission electron microscopy (TEM). In Fig. 4(a), the gradually shift of GeSn peaks in HRXRD indicates the increase of Sn composition. The results show GeSn with Sn compositions from 1% to 7% (Note, the sample with 5% Sn is not shown due to low quality). In Fig. 4(b), the RSM shows that the GeSn layer is strain relaxed grown on Si substrate. In Fig. 4(c), the TEM image shows that the misfit dislocations are localized at GeSn/Si interface.
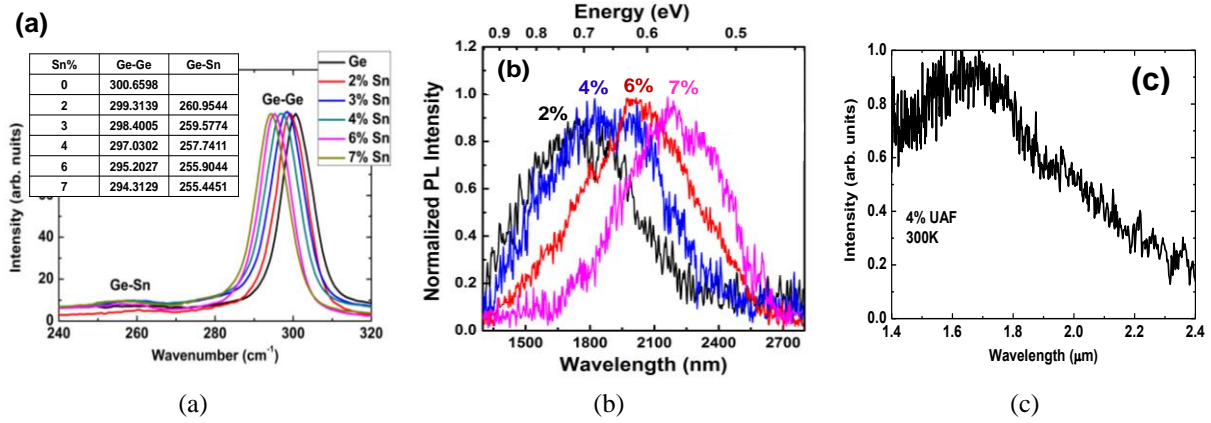
9

Fig. 5. (a) Raman spectra of the GeSn films. The shift in Ge-Ge peak results from the incorporation of Sn in Ge lattice which changes the bond size of Ge-Ge lattice. Ge-Sn peaks are shown at lower wavenumber due to a weaker bond. (b) Room temperature photoluminescence spectra of the GeSn films with Sn compositions of 2, 4, 6, and 7 %. Incorporation of Sn has shifted bangap towards lower energies. (c) Room temperature photoconductor spectrum response for a device fabricated using a 4% GeSn sample.

Optical characterization of the GeSn samples has been performed using Raman and photoluminescence (PL) spectroscopy as shown in Fig. 5(a) and (b), respectively. Fig. 5(a) shows that the Ge-Ge peak in the GeSn films are shifted to lower wavenumbers due to the induced strain by incorporation of Sn atoms. The Ge-Sn peaks for different Sn mole fractions are observed at 250-260 cm^{-1} also shown in the figure. Fig. 5(b) shows the normalized PL emission for different samples. From the spectrum, it is clear that as Sn composition increases, the PL peak shifts toward to longer wavelength as a result of bandgap energy reduction. The sample with 4% Sn has been fabricated into photoconductor devices. The device spectrum response at 300K is shown in Fig. 5(c) with response going beyond standard Ge detector long wavelength cut-off and extending to 2.4 μm. The longer wavelength response beyond the material bandgap is attributed to thermal effect and defects.
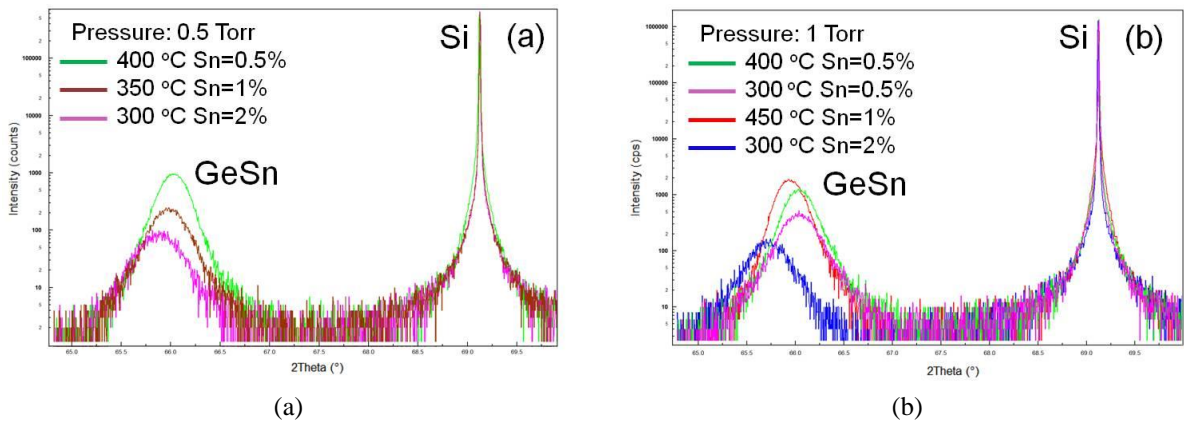

Fig. 6. 2θ-ω scan of GeSn using SnD$_4$ as Sn precursor. Material growth at different temperatures at the pressure of (a) 0.5 Torr and (b) 1 Torr. The GeSn peak shifts to lower angle as Sn composition increases.

We have conducted study of GeSn growth using SnD$_4$ as Sn precursor. Since SnD$_4$ is fairly unstable at the room temperature, the vendor (Voltaix) initially could not guarantee the gas

quality. The team has come out a solution to obtain the SnD_4 with a low temperature package, which could maintain it to be chemically stable but it is in liquid phase. A special gas cabinet was built with a Dewar (filled with dry ice) to bring the SnD_4 cylinder to around -50°C so that a stable vapor gas pressure could be maintained. Then Argon gas was brought in to mix with SnD_4 and the mixed gases were delivered to the growth chamber through a mass flow controller (MFC). This gas delivery method is manufacture friendly.

Due to the fast decomposition of SnD_4 in the delivery line and MFC walls, the flow rate readings are not accurate. Therefore, a pressure-based system is adopted for accurate measurement of SnD_4 flow as well as all other precursors and Ar. The deposition pressure of the system is controlled by a throttle valve which is placed before the turbo-pump. In order to calibrate the flow rates with the deposition pressure in the system, the throttle valve is place at different positions and the flow rates of the gases can be changed. For example, at 1% open position of the throttle valve, the flow rate of Ar has changed from 1 to 25 sccm and the corresponding pressure has been recorded. The same procedure has been adopted for germane and silane. The partial pressures of all gases are measured by capacitance monometer pressure gauge in the vacuum chamber. In order to determine the partial pressure of SnD_4 a needle valve is placed on the delivery line to control the gas flow in the chamber (Figure 7). In addition, SnD_4 is kept in the temperature around -50 °C to maintain its liquid form. The vapor pressure of the gas is led to the chamber through a needle valve. By opening the needle valve at different positions, the partial pressure of the gas is controlled from 0 to 1.5 mTorr. After recording all the partial pressures for different gases, the chamber is set to the desired pressure and temperature the experiments are carried out under different conditions. The typical temperature range was set to 300-450 °C and the deposition pressure was kept between 0.1 to 10 Torr.
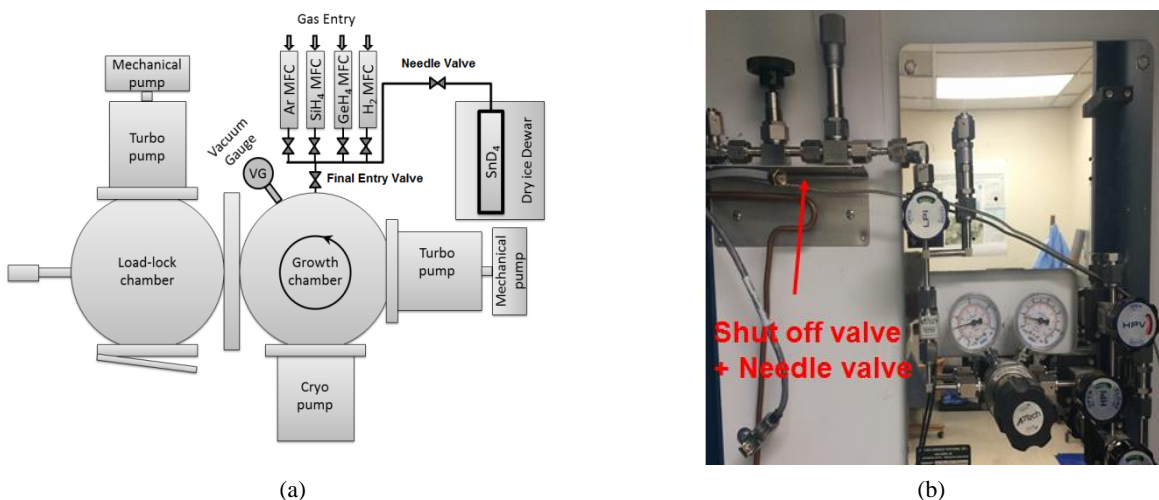

(a)   (b)

Fig. 7. (a) Cold wall UHV-CVD system with SnD_4 in-situ gas mixing. The samples are loaded in the load-lock chamber and after pumping down to 10-8 Torr pressure it is transferred to the growth chamber. The growth chamber is pumped down with a turbo-molecular pump and a cryogenic pump. Gases are entered in the chamber through a MFC and a final entry valve. The SnD_4 gas is kept in dry ice Dewar and the vapor pressure is mixed with the gases before entering the chamber through a needle valve. Partial pressure of SnD_4 gas as well as silane, germane and argon are measured by a vacuum gauge. (b) The needle valve is placed after the gas regulators in order to control the SnD_4 flow.

Analysis of Sn mole fraction of the GeSn films has been performed using high resolution X-ray diffraction (HRXRD). Fig. 6(a) and (b) show the 2θ-ω scan of GeSn thin films grown on Si at the pressures of 0.5 and 1 Torr using SnD_4, respectively. The growth temperature was also shown in the figures, which was kept below 450 °C to be compatible with a Si complementary metal-oxide-semiconductor (CMOS) process. The GeSn peaks shift toward lower angle in HRXRD indicating the increase of Sn composition. The growth has conducted with chamber pressure from 0.1 to 1 Torr. The GeSn growth does not require a prior growth a Ge buffer layer.

(a)   (b)
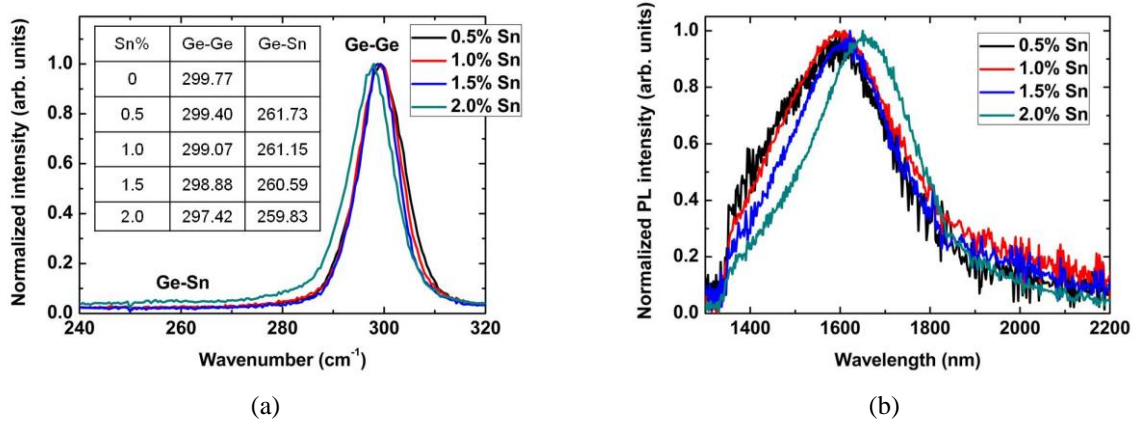
Fig. 8. (a) Raman spectra of the GeSn films. Inset: peak positions of Ge-Ge and Ge-Sn. (b) Room temperature photoluminescence spectra of the GeSn films with Sn compositions from 0.5 to 2 %.

Optical characterization of the GeSn samples has been performed using Raman and photoluminescence (PL) spectroscopy as shown in Fig. 8(a) and (b), respectively. In Fig. 8(a), the Ge-Ge peaks in the GeSn films are shifted toward lower wavenumbers due to the induced strain by incorporation of Sn atoms. The Ge-Sn peaks also shift toward lower wavenumbers as Sn composition increases. The summarized peak positions are shown in Fig. 8(a) inset. Fig. 8(b) shows the normalized PL emission from GeSn films with Sn compositions from 0.5 to 2%. As Sn composition increases, the PL peak shifts toward longer wavelength (from 1583 nm of 05% Sn to 1648 nm of 2% Sn) as a result of bandgap energy reduction.
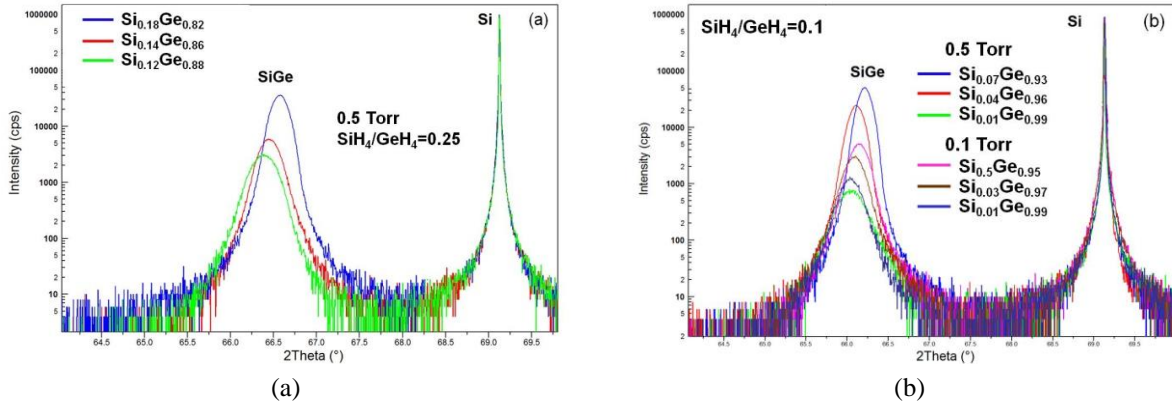
Growth and characterization of SiGe

(a)   (b)

Fig. 9. 2θ-ω scan of SiGe. (a) $SiH_4/GeH_4=0.25$ and pressure of 0.5 Torr. (b) $SiH_4/GeH_4=0.1$ and pressure of 0.5 and 0.1 Torr.

In order to demonstrate growth of SiGeSn, the study of SiGe growth was firstly conducted (followed by the Sn incorporation to finally achieve SiGeSn growth). The growth mechanism has been investigated and the results are summarized in below.

Figure 9 shows the 2θ-ω scan of SiGe thin films. At high SiH_4/GeH_4 ratio of 0.25, the Si compositions are from 12 to 18%, as shown in Fig. 9(a). At low SiH_4/GeH_4 ratio of 0.1, the Si composition varies from 1 to 5 % at pressure of 0.1 Torr and from 1 to 7 % at pressure of 0.5 Torr, respectively, as shown in Fig. 9(b). Increase in SiH_4/GeH_4 ratio and chamber pressure results in higher Si incorporation. Furthermore, the Si composition increases as growth temperature increases. All growth temperatures in this study were kept below 450 °C.

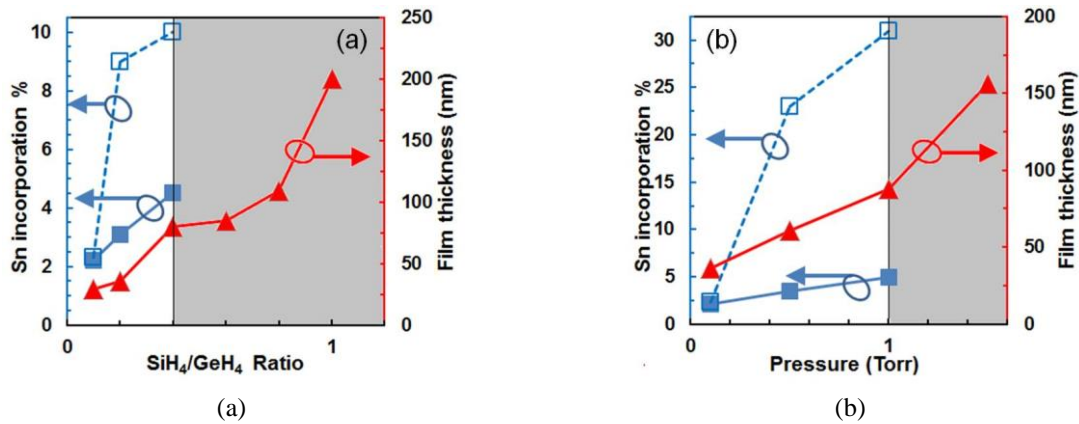**Growth and characterization of SiGeSn**

Fig. 10. SiGeSn growth mechanism. (a) Sn incorporation percentage and film thickness as the functions of gas flow ratio. The fixed deposition pressure is 0.1 Torr and the fixed ratio of $SnCl_4/GeH_4$ is 0.2. (b) Sn incorporation percentage and film thickness as the functions of deposition pressure. The fixed gas flow ratio of $SiH_4/GeH_4/SnCl_4=2/10/1$. The solid and dashed lines show substitutionally incorporated Sn and total incorporated Sn in SiGe lattice, respectively.

The growth of SiGeSn has been successfully demonstrated. The SiH_4, GeH_4 and $SnCl_4$ are used as Si, Ge and Sn precursors, respectively. The study of growth mechanism has been conducted, as shown in Fig. 10. Fig. 10(a) shows the SiGeSn growth at different SiH_4/GeH_4 ratios. The pressure is fixed at 0.1 Torr and $SnCl_4$ flow was fixed as $SnCl_4/GeH_4=0.2$. Increase in SiH_4 flow results in increase in Sn incorporation. The solid and dashed lines show substitutionally incorporated Sn and total incorporated Sn in SiGe lattice, respectively. The deviation of two curves indicates that part of Sn interstitially incorporated into the SiGe lattice. Fig. 10(b) shows SiGeSn growth results at different chamber pressures. The fixed gas flow ratio is of $SiH_4/GeH_4/SnCl_4=2/10/1$. Increase in chamber pressure results in higher Sn incorporation in the film. Growth starts at 0.1 Torr and continues until the pressure reaches 1 Torr. When the pressure is higher than 1 Torr, the films become amorphous.
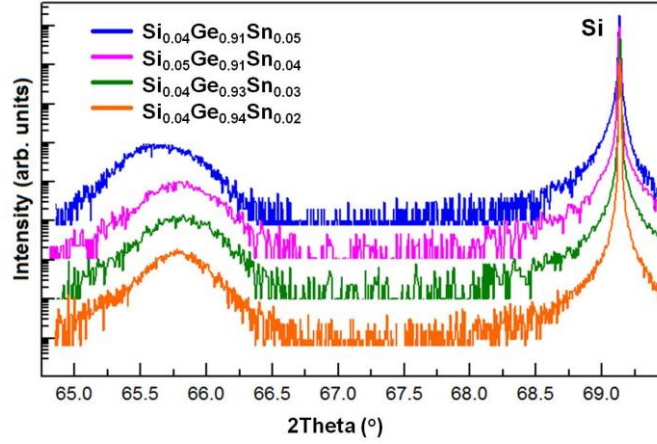
Fig. 11. 2θ-ω scan of SiGeSn films using $SnCl_4$ as Sn precursor. The peak at 69° is attributed to Si substrate and the peaks between 66.5-65° belong to SiGeSn films.

Figure 11 shows the 2θ-ω scan of SiGeSn thin films using $SnCl_4$ as Sn precursor with Sn compositions from 2 to 5 %. The Si composition was kept as 4 % (except a little higher one in $Si_{0.05}Ge_{0.91}Sn_{0.04}$). As Sn composition increases, the SiGeSn peak gradually shifts toward lower angle. Compared to GeSn samples (the same Sn composition), these peaks are closer to the Si peak due to the Si incorporation. Therefore, the incorporation of Si and Sn in Ge can be identified by the spectra behavior abovementioned.
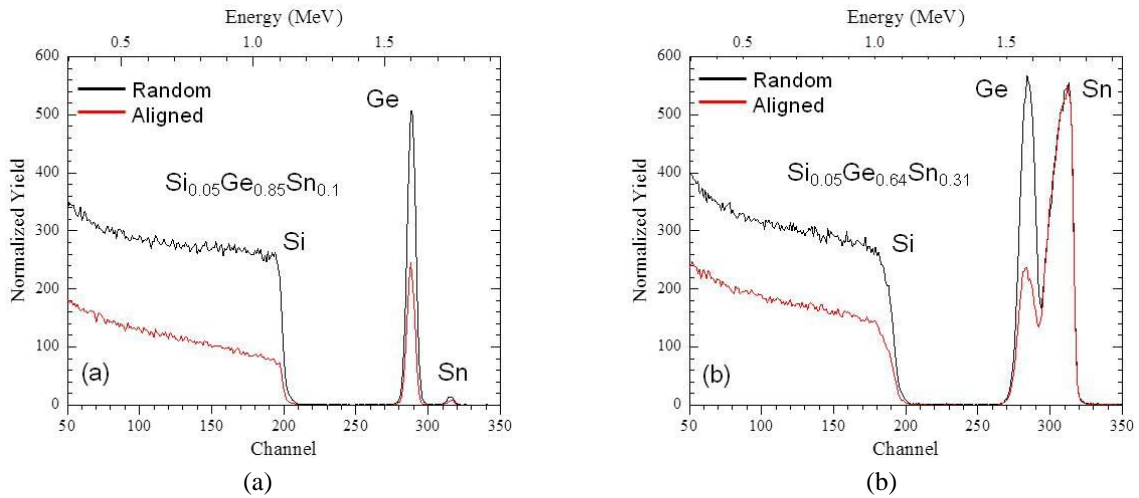

Fig. 12. Rutherford backscattering (RBS) spectra for (a) $Si_{0.05}Ge_{0.85}Sn_{0.1}$ and (b) $Si_{0.05}Ge_{0.64}Sn_{0.31}$. The black and red curves are random and aligned spectra, respectively.

Rutherford backscattering (RBS) spectra were used to identify the elemental content. Two representative SiGeSn samples are shown in Fig. 12. The black and red curves are random and aligned spectra, respectively. The ratios of peak heights for Si and Ge indicate that Si occupies substitutional lattice sites. On the other hand, the ratio of Sn peak heights reveals that not all of Sn atoms are substitutionally incorporated; some of them are interstitially incorporated into the SiGe lattice. The total incorporated Sn compositions shown in Fig. 12 are 10% and 31%, respectively. According to XRD measurement results, the corresponding substitutionally

incorporated Sn compositions are 4% and 5%, respectively. The material quality needs to be further improved. The work of optimizing the growth condition is currently underway.

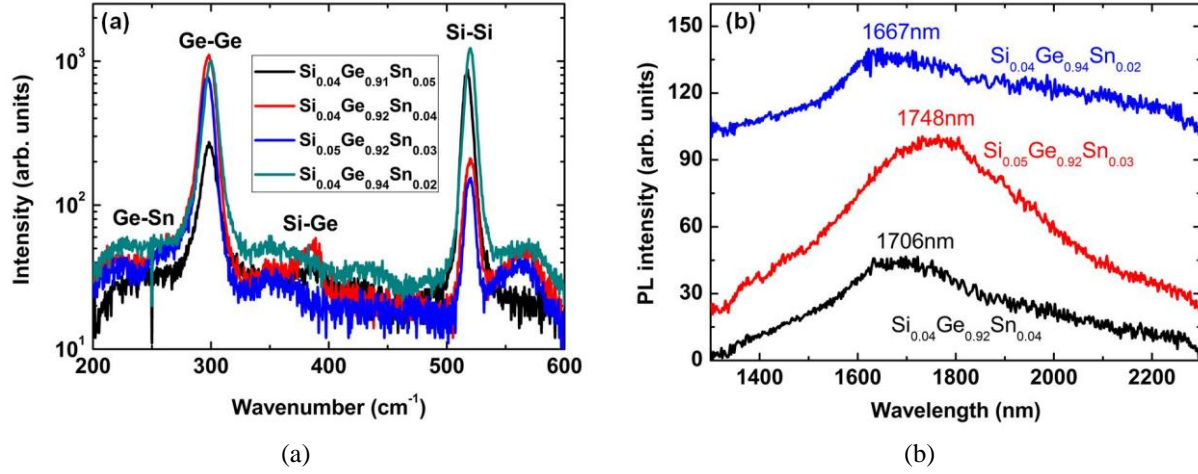(a)   (b)

Fig. 13. (a) Raman spectra of the SiGeSn films. (b) Room temperature PL emissions from SiGeSn samples. Each spectrum is stacked for clarity.

Figure 13(a) shows the Raman spectra of the SiGeSn films. The shifts in Si-Si and Ge-Ge bonds are due to the incorporation of Si and Sn in the Ge lattice. The Si-Ge peaks are located between the Si-Si and Ge-Ge peaks and the Ge-Sn peaks are shown at lower wavenumbers than the Ge-Ge peaks. The peak positions are summarized in Table III. Some Si-Ge and Ge-Sn peaks cannot be identified due to the low intensity in Raman spectra.

Table III Peak positions of Si-Si and Ge-Ge extracted from Fig. 13(a)

Sample	Si-Si	Ge-Ge	Si-Ge	Ge-Sn
Reference	522.357	300.006		
$Si_{0.04}Ge_{0.91}Sn_{0.05}$	520.526	297.588	399.096	
$Si_{0.04}Ge_{0.92}Sn_{0.04}$	520.156	297.861	398.735	259.538
$Si_{0.05}Ge_{0.92}Sn_{0.03}$	519.723	297.895		259.965
$Si_{0.04}Ge_{0.94}Sn_{0.02}$	519.876	299.695		260.006

Room temperature PL emissions from SiGeSn samples are shown in Fig. 13(b). Each spectrum is stacked for clarity. The incorporation of Sn reduces the bandgap energy, which on the contrary is increased by the incorporation of Si. Therefore, the PL peak position is determined by both Si and Sn compositions.

Figure 14 shows the comparison of 2θ-ω scans between SiGe, SiGeSn and GeSn samples. It is clear that the Si and Sn compositional-dependent peak positions agree well with theoretical predication.
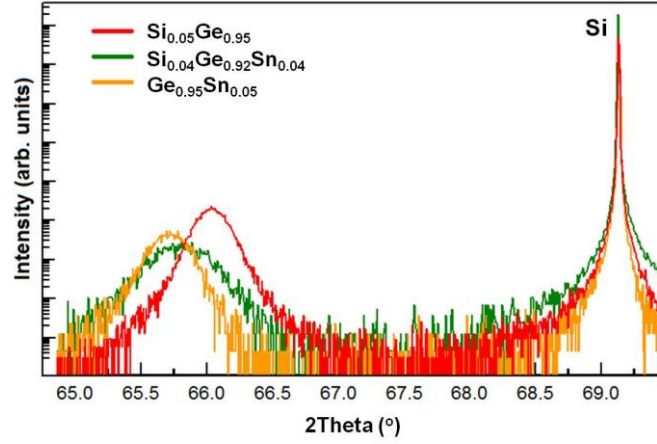
Fig. 14. Comparison of 2θ-ω scans between SiGe, SiGeSn and GeSn samples. The incorporating of Si in the film shifts the peak toward to Si substrate peak, while incorporating of Sn shifts the peak away from the Si substrate peak, which agrees well with theoretical study.
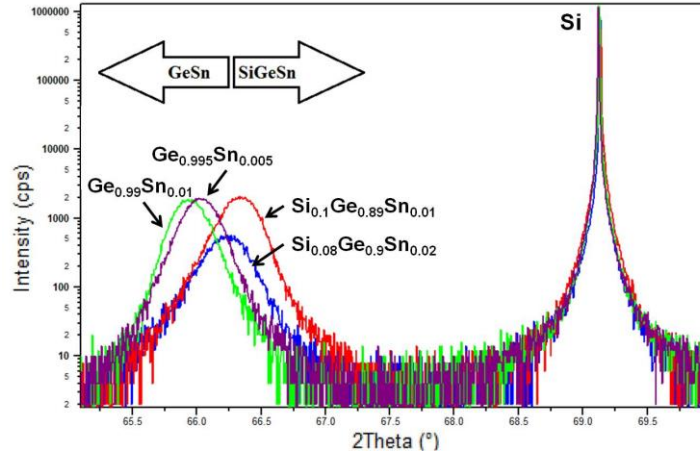

Fig. 15. 2θ-ω scan of SiGeSn and GeSn films. The peak positions follow the theoretical study.

We have also conducted preliminary study of SiGeSn growth using SnD_4 as Sn precursor. The 2θ-ω scans of SiGeSn and GeSn films using SnD_4 as Sn precursor are shown in Fig. 15. The change of the peak positions follows the theoretical predication.

In order to optimize the growth conditions for the growth of high quality material needed for photodetectors, a two-step method is adopted to suppress the propagation of defects in the first layer. The initial step is a low temperature (LT) growth below 400 °C and the second step is a high temperature (HT) growth above 500-650 °C. The two-step (LT:HT) growth method adopted for the growth of Ge and the role of pressure and different carrier gases (Ar, N_2, and H_2) is presented. Silicon-germanium films were grown in a single step at 350-450 °C and the role of pressure in increasing the material quality and Si incorporation at low temperature growth was studied.

In order to achieve higher material quality, the high-quality Ge growth parameters have been used to benchmark GeSn growth. However, it was observed that usage of stannic chloride

resulted in the etching of the films as they were grown. This etching behavior was attributed to the production of HCl which is an etchant of Ge. Therefore, no growth was observed in high flow rates of stannic chloride. In order to improve the film quality, low flow rates of stannic chloride and higher flow rates of GeH_4 were used. The grown samples were characterized using different characterization methods such as Raman, PL, Ellipsometry.
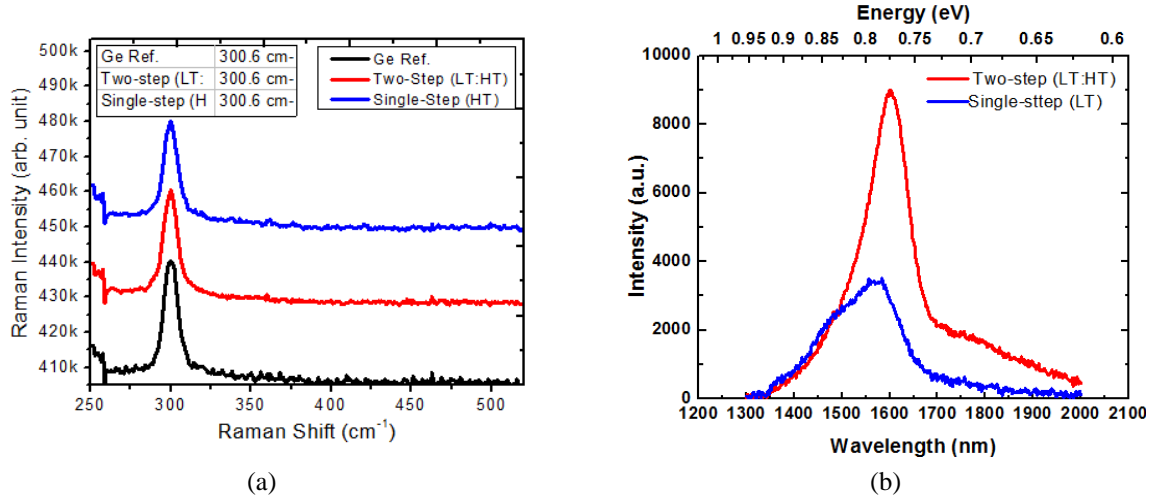

(a)   (b)

Fig. 16. (a) Raman spectroscopy measurements of the two-step (LT:HT) at 400:600 °C and the single-step (HT) at 600 °C growth shows standards Ge peak for both growths. (b) Photoluminescence spectroscopy measurements of the two-step (LT:HT) at 400:600 °C and the single-step (HT) at 600 °C growth shows higher PL intensity in a two-step growth.

Fig. 16 shows the Raman and PL spectra of Ge films grown in a two-step (HT:LT) and single-step (HT) growth at a fixed growth pressure of 1 torr. For GeSn growth, a single step GeSn growth is adopted and the layers are grown without using a buffer layer. The films were grown using GeH_4 and $SnCl_4$ as Ge and Sn precursors, respectively.
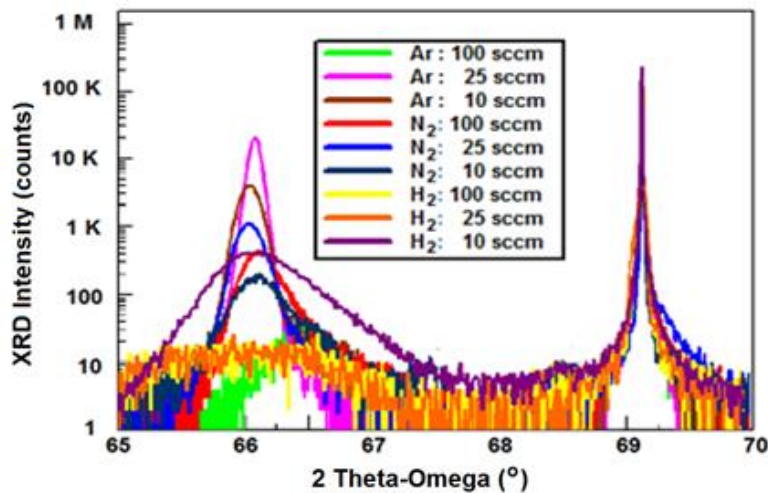

Fig. 17. The XRD patterns obtained from (004) plane of the Ge films grown on Si at different flow rates of Ar, H_2, and N_2 carrier gases.

17

Fig. shows the result of the 2Theta-Omega XRD scan from 004 plane. The peaks located at 69° belong to Si substrate and the peaks observed at 66° belong to Ge epi-layer. All the plots were normalized on the Si peak by dividing the Ge peak intensity by Si peak intensity (Ge/Si peak intensity), so that the Ge peaks could be compared. Comparison of peak intensity and full width at half maximum (FWHM) of the samples grown using H_2 carrier gas show that at 10 sccm H_2 flow rate the FWHM was 0.62°. At flow rates of 25 and 100 sccm, the peaks had lower intensity and higher FWHM, ~2°. Using nitrogen and argon as carrier gas resulted in films with higher intensity and lower FWHM. However, Ge films grown with Ar showed higher intensity in comparison with N_2 and FWHM of 0.1° which was less than half of that of using N_2 carrier gas (0.25°).
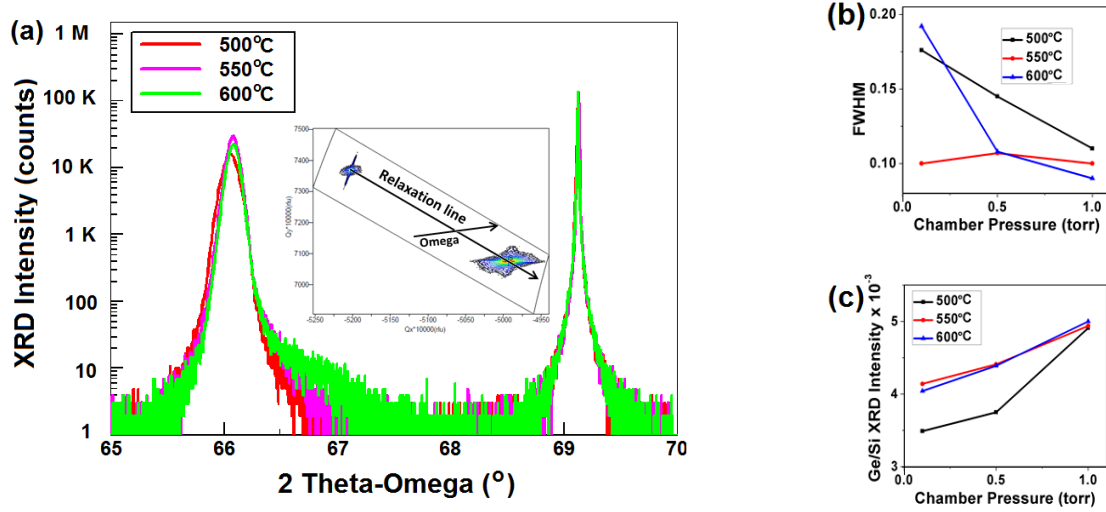

Fig. 18. The XRD analysis of Ge films grown in two steps (LT:HT). (a) The XRD patterns of Ge films at fixed GeH$_4$ and Ar flow rate. RSM of the Ge film grown at 550 °C shows 0.06% tensile strain (inset). (b) FWHM of the peaks was decreased by reduction of temperature and pressure. (c) Ge/Si peak intensity increased by increasing the growth temperature and pressure.

Fig. (a) shows the 2Theta-Omega XRD characterization of the two-step growth (LT:HT) at 0.5 torr. The LT step was kept at 300 °C and the HT step was performed at 500, 550, and 600 °C. Fig. (b) and (c) show the change in the FWHM of Ge peaks and normalized Ge peak intensity for different growth pressures (0.1 to 1.0 torr) and HT step temperatures (500 to 600 °C), respectively. The results show that increasing the pressure resulted in higher Ge peak intensity as well as lower FWHM. A large difference was observed between the intensity and FWHM of the growth at 500 °C and the growth at 550 °C and 600 °C at lower pressures. However, the difference was minimized by increasing the pressure to 1.0 torr. Achieving higher Ge intensity and lower FWHM showed that high quality Ge could be grown at 50 to 100 °C lower temperatures if the pressure was increased from 0.1 to 1.0 torr. The measured thickness of the films grown at 550 °C showed that the film thickness increased from 1188 nm at 0.1 torr pressure to 2734 nm at 1.0. This was mainly due to the increase in the residence time of the precursors in the chamber at higher pressures which led to an increase in the growth rate.
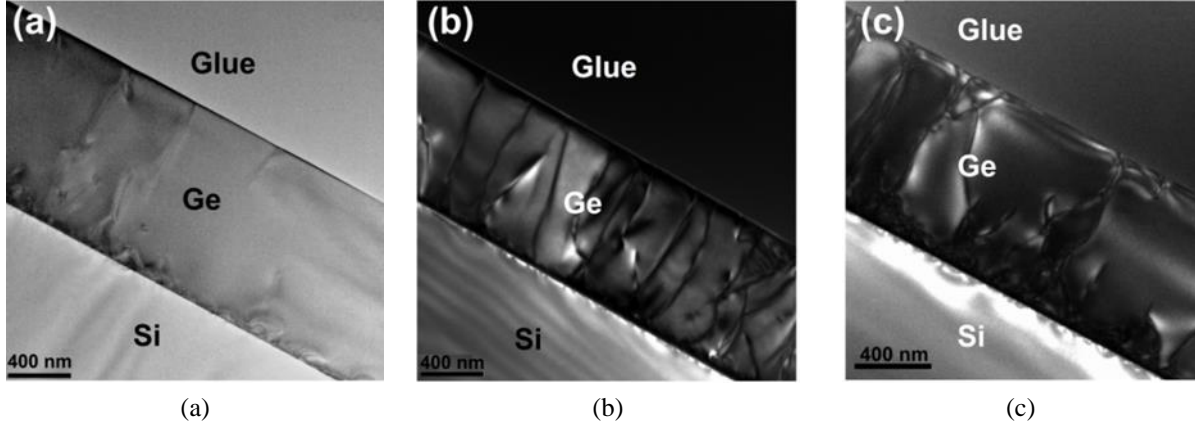
Fig. 19. TEM micrograph of the Ge films grown at different growth conditions (a) Two-step (LT: 300 °C, HT:550 °C) growth using Ar carrier gas. b) Single-step growth at 550 °C using Ar carrier gas. (c) Two-step (LT:300 °C, HT:550 °C) growth using H_2 carrier gas.

Fig. (a) displays the TEM characterization results of the Ge films which shows high material quality was achieved in the two-step growth method using Ar carrier gas. In order to compare the effect of a single step growth with a two-step growth, the TEM of a Ge layer that was grown at 550 °C without growing the Ge buffer layer at 300 °C is shown in Fig. (b). In addition, the TEM image of a two-step growth of Ge using H_2 carrier gas is presented in Fig. (c). The threading dislocation density of the two-step Ge growth using Ar was measured to be as low as 1.3×10^7 cm^{-2}. A single step growth increased the TDD to 8.5×10^8 cm^{-2} and the growth using hydrogen also resulted in highly defective film with a TDD average of 5.0×10^8 cm^{-2}.

The TDD of the Ge films was determined using etch pit measurement and compared with the results achieved from TEM measurement. The comparison of TDD using TEM (1.3×10^7 cm^{-2}) and etch pit measurements (1.7×10^7 cm^{-2}) for Ge films confirmed the accuracy of the measurements.

In order to demonstrate high quality growth of GeSn, the best growth mechanism with the flow of Argon as carrier gas has been conducted. The growth mechanism has been investigated and the results are summarized in below.

Fig. (a) shows the XRD pattern from (004) plane of GeSn films with and without Ar carrier gas. After normalizing the Si peaks, the GeSn peaks were compared. The intensity of the GeSn peak showed an increase by approximately one order of magnitude after adding Ar as the carrier. In addition, FWHM of the GeSn peaks decreased from 0.31 to 0.24 degrees. Fig. (b) and (c) compares the typical TEM of GeSn samples grown without and with Ar carrier gas, respectively. The enhancement in the quality of material is observed by comparing the two figures. A higher density of threading dislocations and stacking faults was observed in the growth without Ar carrier gas. The asymmetrical RSM scan of the samples from (-2-24) plane show that samples were strain relaxed but the GeSn peak in the growth without Ar carrier gas had lower intensity. The spread observed in the omega direction was due to the mosaicity of the film as a result of strain relaxation. The comparison between the RSMs of samples without (Fig. (d)) and with (Fig. (e)) Ar carrier gas showed larger mosaic spread for the growth without Ar carrier gas.
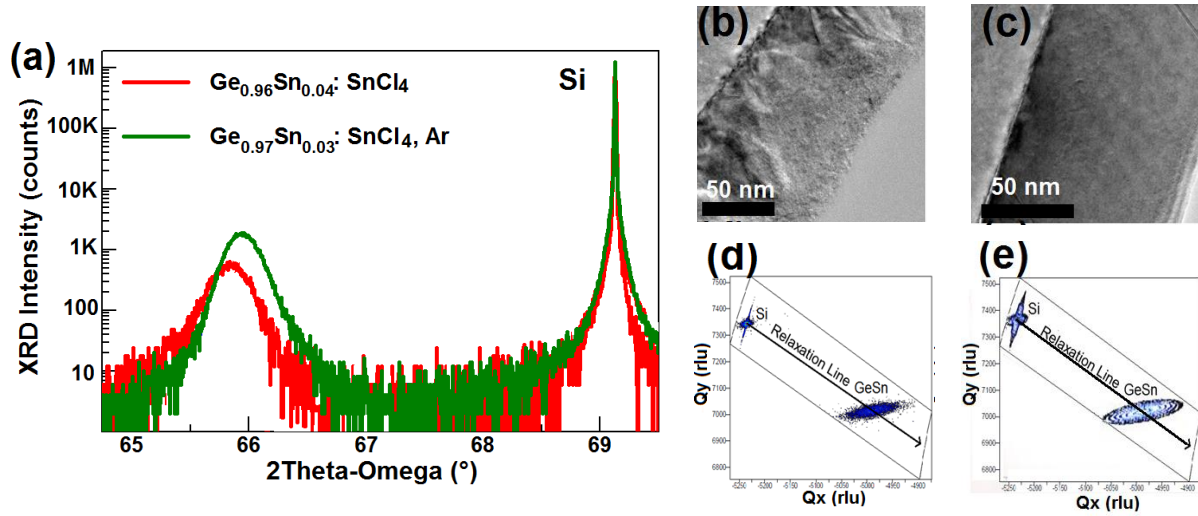
Fig. 20. Material characterization of GeSn films grown with and without Ar carrier gas. (a) 2Theta-Omega XRD scan of the GeSn samples. (b) Cross sectional TEM image of GeSn film grown without and (c) with Ar carrier gas. (d) The RSM scan of GeSn film grown without and (e) with Ar carrier gas.
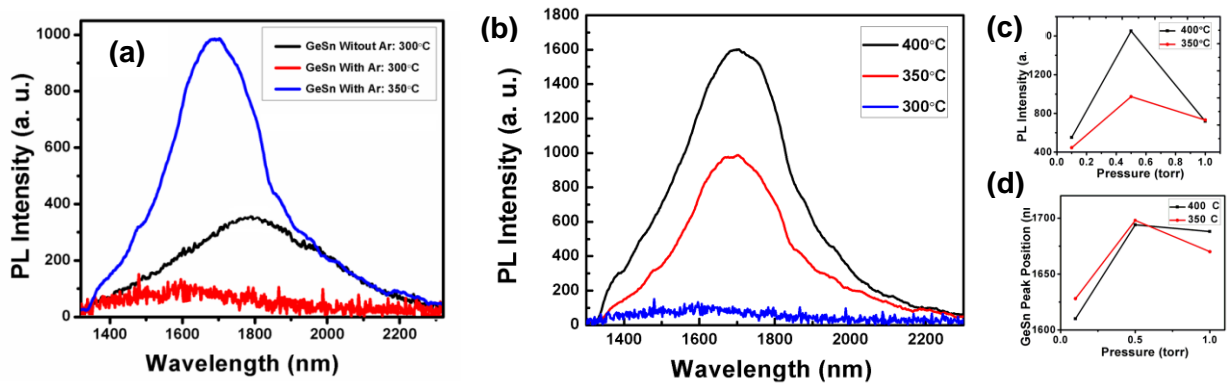

Fig. 21. Comparison of PL emission from samples grown with and without Ar carrier gas.

Fig. (a) shows PL characterization of the GeSn samples grown with and without Ar at 300 °C and 350 °C. The growth pressure was kept at 0.5 torr for all samples. The PL intensity of the material grown at 300 °C without a carrier gas showed higher intensity than the one grown with Ar. However, no growth was observed above 300 °C without Ar carrier gas. For GeSn growth at 350 °C with Ar carrier gas, approximately three times higher intensity was observed which indicates higher quality of the grown material. This increase in the material quality could be attributed to higher mobility of Ge ad-species at higher temperatures and the role of Ar carrier gas to act as a surfactant to further increase the surface mobility due to its large atomic size. The PL peak positions of all samples were shifted from the Ge characteristic indirect peak at 1550 nm towards longer wavelengths. This shift indicated incorporation of Sn in Ge lattice. The comprehensive study on the growth at different temperatures and pressures showed that GeSn material growth using Ar as carrier gas was possible at temperatures higher than 300 °C. Fig. (b) shows the PL measurement of the $Ge_{0.98}Sn_{0.02}$ films at growth pressure of 0.5 torr. The integrated PL intensity and peak position of the growth at different pressures and temperature are shown in Fig. (c) and (d), respectively.
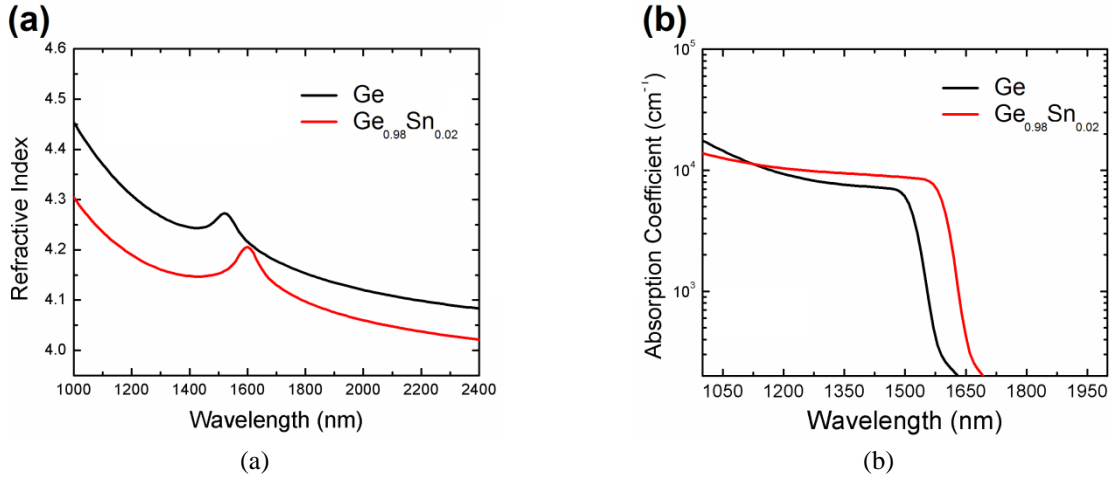
Fig. 22. Optical charactrization of the $Ge_{1-x}Sn_x$ samples using spectroscopic ellipspmetry. (a) Refractive index and (b) absorption coefficient of Ge and $Ge_{0.98}Sn_{0.02}$ sample grown at 350 °C temperature and 1 torr chamber.

Fig. shows the measured refractive index and absorption coefficient for a $Ge_{0.98}Sn_{0.02}$ sample grown at 350 °C, $SnCl_4$ flow of 0.5 sccm, and growth pressure of 1 torr. The characterization result is compared to Ge bulk characteristic from 1000 to 2400 nm wavelength. The bandgap edge of the $Ge_{0.98}Sn_{0.02}$ sample resulted in a shift in the characteristic curve of the GeSn sample towards longer wavelength in comparison with Ge. Due to the increase in the absorption coefficient towards longer infrared wavelengths, the GeSn devices can operate at longer wavelengths.
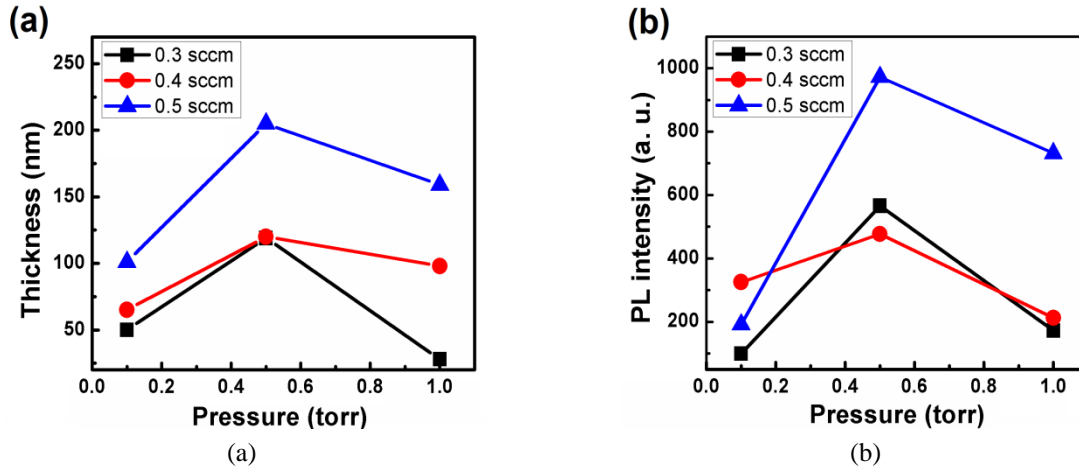

Fig. 23. Film thickness and PL intensity of GeSn films as a result of deposition pressure change. (a) Change in the thickness and (b) PL intensity of the GeSn samples grown for different flow rates of $SnCl_4$ at growth pressures of 0.1 to 1 torr at 350 °C growth temperature.

Measurement of film thickness using spectroscopic ellipsometry technique was performed to understand the growth mechanism of the films at different conditions. Fig. (a) shows the thickness measurement of the samples grown at 350 °C and 0.5 torr with flow rates of $SnCl_4$ from 0.3 to 0.5 sccm. The film thickness for all samples showed an increase from 0.1 torr to 0.5

torr but the thickness decreased above 0.5 torr. The increase in the film thickness at higher pressures was the result of higher residence times of ad-species. However, as discussed in the PL section, increased pressure resulted in a higher decomposition rate of $SnCl_4$ with respect to GeH_4 due to lower bond energy of the molecules. Such higher decomposition rate resulted in higher production rate of HCl according to a previously discussed reaction. High pressure results in more GeH_4 etching because $SnCl_4$ decomposition produces four HCl molecules which can etch four Ge atoms from crystal sites. Dominance of etching results in lower film thickness and lower material quality which results in lower PL intensity as can be seen in Fig. (b).

GeSn samples from ASM: Our collaborator ASM Company provides us GeSn samples grown using an ASM Epsilon® 2000 Plus reduced pressure chemical vapor deposition (RPCVD) system using $SnCl_4$ and GeH_4 as precursors.

We have conducted detailed study on GeSn materials from ASM. The Sn concentrations are measured by secondary ion mass spectroscopy (SIMS) and checked by Rutherford backscattering spectroscopy (RBS) and Raman spectroscopy; The material background doping is confirmed by room and low temperature hall; The Sn compositional-dependent refractive index is obtained by ellipsometry; The lattice constant and strain are measured by X-ray diffraction (XRD); The film thickness, defect formation and propagation are investigated by high resolution transmission electron microscopy (HR-TEM); And the sample surface profile is examined by atomic force microscopy (AFM). These results are summarized in Fig. 24.
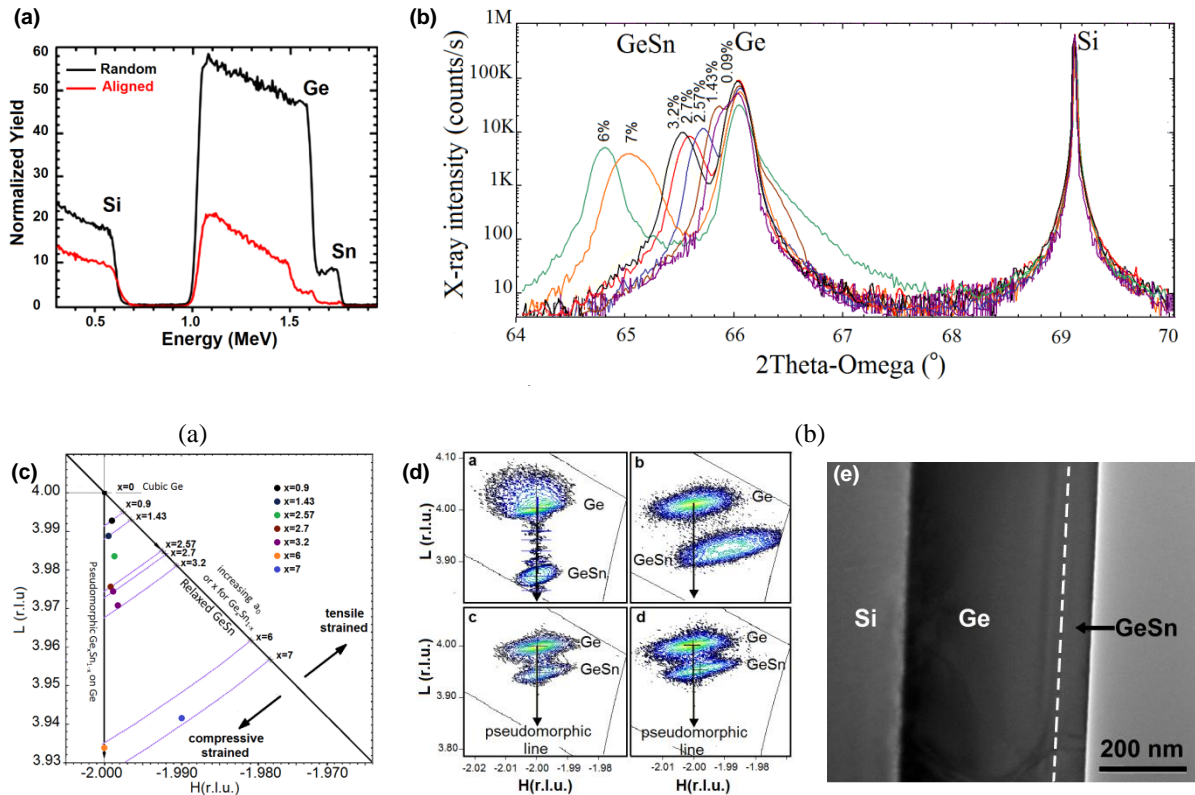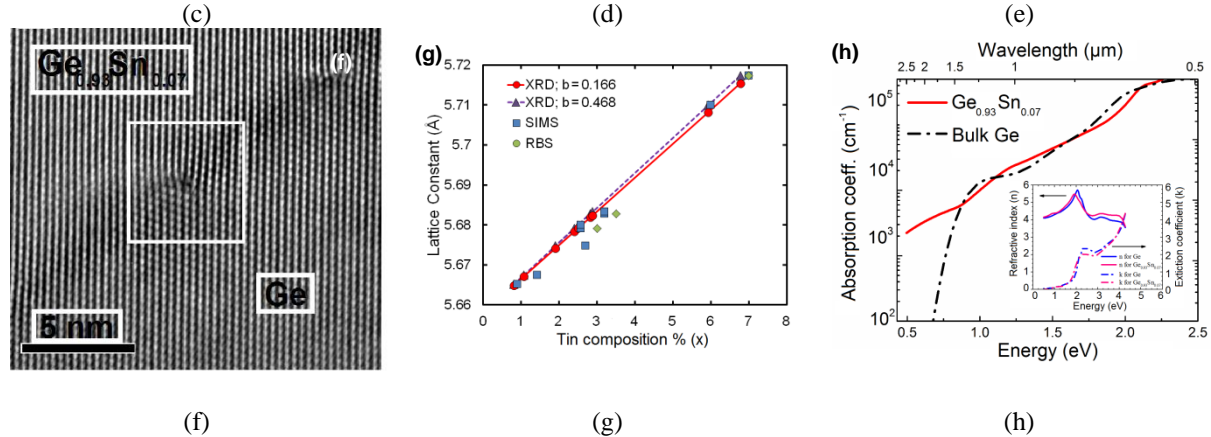
Fig.24 (a) Random (black) and Si (001) aligned (red) RBS spectra of $Ge_{0.93}Sn_{0.07}$ with the thickness of 240 nm on Ge buffer layer. (b) The XRD rocking curve measurement (2θ-ω scan) of $Ge_{1-x}Sn_x$/Ge films which is performed along symmetric (004) plane. The peak at 69° shows Si substrate peak and the peaks between 66-64° belong to Ge buffer layer and $Ge_{1-x}Sn_x$ films. Larger out-of-plane lattice constant satisfy Bragg's law at lower angles. (c) Sketch of reciprocal space map from assymetrical plane (-2 -2 4) for different $Ge_{1-x}Sn_x$ samples. The x-coordinate shows out-of- plane lattice constant and y-coordinate shows in-plane lattice constant in units of H (=2) and L (=4) for Ge buffer layer, respectively. (d) Reciprocal Space Maps from (-2 -2 4) plane of GnSn film with (a) 6 %, (b) 7 % Sn. Higher Sn content along with higher thickness has resulted in strain relaxation in 7 % Sn sample. The (-2 -2 4) RSM of 3.2 % Sn samples are shown for two different thicknesses of (c) 76 nm and (d) 128 nm. Increase in the thickness of the films results in more relaxation from 16 % to 30 %. Downward arrow shows the pseudomorphic line which is 0 % relaxation. The x-coordinate shows out-of-plane lattice constant and y-coordinate shows in-plane lattice constant in units of H (=2) and L (=4) for Ge buffer layer, respectively. (e) Cross sectional TEM image of Si/Ge/$Ge_{.94}Sn_{.06}$ film shows threading dislocations are trapped on Ge/GeSn interface. No misfit dislocations can be seen on GeSn/Ge interface since thickness of $Ge_{1-x}Sn_x$ layer is less than critical thickness for 6 % Sn alloy. (f) High resolution-TEM image delineates a misfit dislocations at the interface of Ge/$Ge_{.93}Sn_{.07}$ film. (g) GeSn lattice constant of the films vs. Sn composition of $Ge_{1-x}Sn_x$ alloys measured by XRD, SIMS and RBS. Two different bowing factor of 0.468 and 0.166 nm has been used to measure Sn composition of the films through XRD measured lattice constants. Data from SIMS and RBS show offset from the predicted value by Vegard's law. (h) Absorption coefficient of $Ge_{0.93}Sn_{0.07}$ sample is measured at different energies using spectroscopic ellipsometer which shows orders of magnitude higher values at energies below 1 eV in comparison with Ge (especially above 1550 nm wavelength). The inset shows the refractive index (n) and extinction coefficient (k) of $Ge_{0.93}Sn_{0.07}$ film compared to bulk Ge.

II) Optical characterization of GeSn materials

The GeSn samples from our collaborator ASM have been grown using an ASM Epsilon® 2000 Plus reduced pressure chemical vapor deposition system (RP-CVD). Detailed optical study has been conducted.

Photoluminescence (PL) study: The PL measurements were conducted using a continuous wave (CW) laser operating at 532 nm and a Mai Tai® ultrafast laser operating at 690 nm as the excitation sources for temperature and power-dependent study, respectively. Emissions from the sample were collected by an extended InGaAs or PbS detectors.
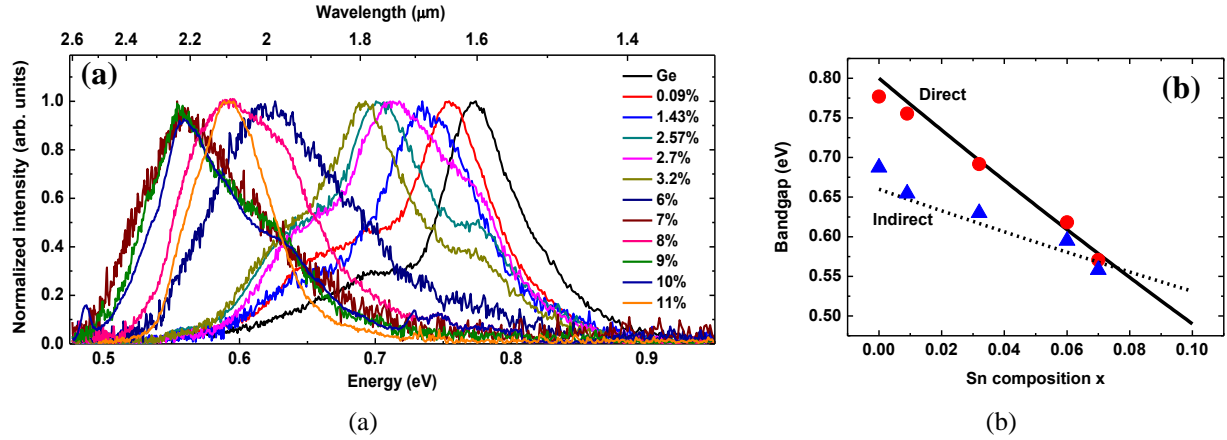
Fig. 25 (a) Room temperature PL spectra (normalized intensity) of the GeSn thin films with Sn compositions from 0% (Ge buffer) to 11%. (b) Direct and indirect bandgap as a function of Sn composition. The black curves are calculated using a standard quadratic equation and the solid points are experimental results.

The Room temperature PL spectra, shown in Fig. 25(a), have a clear composition dependent main peak for each sample, and show a red-shift as the Sn mole fraction increases. All samples are under different compressive strain, which offsets the conduction and valence bands, and consequently further changes the band structure. Based on theoretical calculation, the compressive strain enlarges the direct and indirect bandgap energies. As a result, the position of the peak shifts to higher energy.

As Sn composition increases, the direct bandgap reduces faster than the indirect bandgap, resulting in the continuously reduced separation between the direct Γ-valley and the indirect L-valley in the conduction band, as shown in Fig. 25(b). In the case of high Sn composition samples (Sn% > 6%), the direct and indirect peaks may not be distinguished due to a large spectra overlap. The experimental data agrees with these theoretical calculations. The deviations between theoretical curves and experimental data mainly result from the various compressive strains of the GeSn films. Note that when Sn composition reaches 7% or higher, the bandgap energy of direct becomes smaller than that of indirect, which means the direct bandgap material can be achieved.
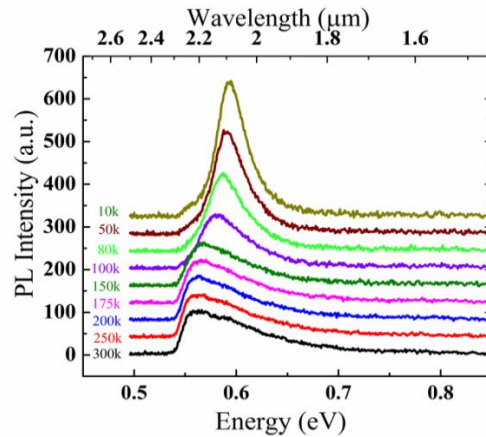

Fig. 26 Temperature-dependent PL measured on $Ge_{0.93}Sn_{0.07}$ illustrates the changes in PL spectra from 10 to 300

24

K. The direct and indirect PL emissions are overlapped and were not discernible.

The temperature-dependent PL spectra of the samples with Sn content of 7 % are shown in Fig. 26. At 10 K, only the indirect peak can be observed while at 300 K the direct peak dominates the PL and indirect peak disappears. The overlapping PL emissions from the direct and indirect bandgaps are high, so the peaks were irresolvable using the Gaussian fitting. It is inferred for this sample with 7 % Sn mole fraction that the direct and indirect energy gaps are almost equal.
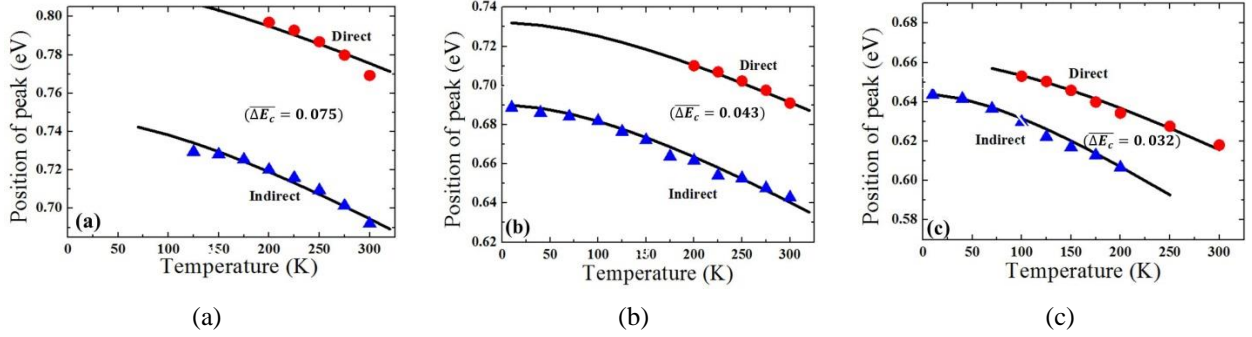

| (a) | (b) | (c) |

Fig. 27 PL peak positions in different temperatures for the direct (red circles) and indirect (blue triangles) for (a) $Ge_{0.991}Sn_{0.009}$, (b) $Ge_{0.968}Sn_{0.032}$, and (c) $Ge_{0.94}Sn_{0.06}$. The Varshni equation is fitted on the PL peak positions for both direct and indirect emissions. Increasing the Sn mole fraction from 0.9 to 6 %, reduces the average distance between the direct and indirect gap $(\overline{\Delta E_c})$ in $Ge_{1-x}Sn_x$ alloy.

The obtained peak positions from fitting process were performed on the extracted PL peaks. The theoretical calculation of peak position versus temperature for a semiconductor can be described by the Varshni relation. The peak positions are plotted as a function of temperature in Fig. 27 for the samples with Sn content of 0.9, 3.2 and 6 %.

We have further investigated the competing between the direct and indirect bandgap transitions. Understanding the competing behavior of PL intensity could provide a strong guidance for the design of future GeSn-based optoelectronic devices.
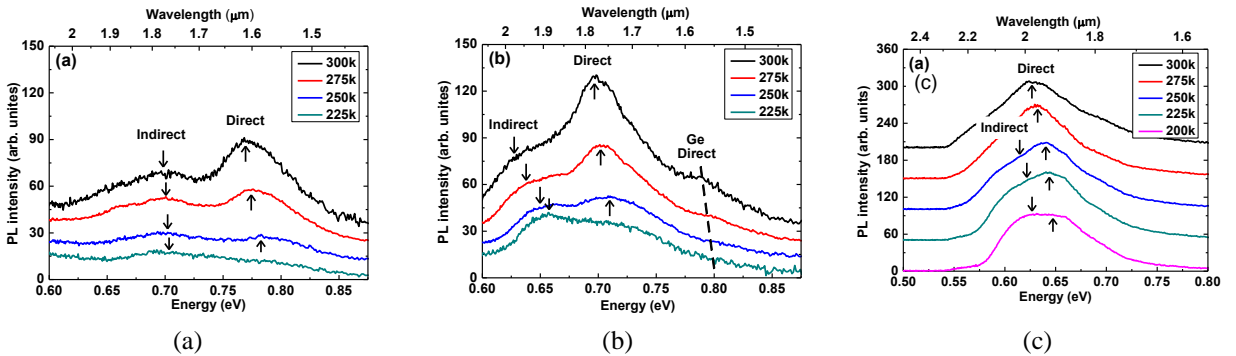

| (a) | (b) | (c) |

Fig. 28 Temperature-dependent PL spectra of (a) $Ge_{0.991}Sn_{0.009}$, (b) $Ge_{0.968}Sn_{0.032}$, and (c) $Ge_{0.94}Sn_{0.06}$. Each curve is stacked for clarity. The direct peaks are marked by upwards arrows, while downward arrows indicate the indirect peaks. In (b), the direct peaks of Ge are labelled by dashed line. The PL intensity increases as temperature increases, and the direct peak grows more rapidly than indirect peak.

Temperature-dependent PL spectra of three samples are shown in Fig. 28. They are indirect material based on material characterization results. In indirect material, the fraction of electron population in L-valley is higher than that in Γ-valley. Since the probability of radiative recombination of direct bandgap transition is higher than that of phonon-assisted indirect radiative recombination, the direct peak can be observed along with the indirect peak. This occurs even when a small fraction of electrons populate the Γ-valley. The obtained PL spectrum is then the superposition of these two peaks. For a given temperature, as Sn composition increases, the bandgap energy separation decreases, which increases the fraction of electrons populated in Γ-valley, therefore enhances the intensity of direct peak. In the case of very small ΔE, the direct and indirect peaks may not be distinguished due to a large spectra overlap. Additionally, for a certain GeSn sample, as temperature increases, which extends the Fermi-tail to higher energy, more thermally excited electrons populate the Γ-valley, resulting in the direct transition dominating the PL at high temperature even with low Sn composition.

A direct bandgap $Ge_{0.9}Sn_{0.1}$ alloy has been identified by temperature-dependent PL study based on the single peak spectrum and the narrow line-width. Room temperature PL emission as long as 2230 nm has also been observed from the same sample.

In Fig. 29(a), the indirect and direct regions correspond to the indirect and direct bandgap materials, respectively. The uncertain region reveals the discrepancy of theoretical calculations due to various models and fitting parameters. Materials located in the uncertain region could be either direct or indirect bandgap material. The insets in indirect and direct regions show the schematic band diagrams of $Ge_{1-x}Sn_x$ alloy and the mechanism of PL spectra formation for indirect and direct bandgap materials, respectively. Fig. 29(b) shows temperature dependent PL spectra of a 10% GeSn sample in which only a single peak with narrowed line-width was observed. This PL linewidth reduction compared with that of lower Sn composition PL (for example 8 and 9%, not shown in this result) in combining with the PL linewith forming mechanism shown in Fig. 29(a) indicating the 10% GeSn is a direct bandgap material. In Fig. 29(c), the line-width of 8 and 9 % Sn samples are nearly twice that of 10% Sn sample at the temperature range from 300 to 100 K, confirming that sample D is a direct bandgap material. In Fig. 29(d), region (i) and (ii) correspond to indirect bandgap material, while region (iii) corresponds to direct bandgap material. The solid and open symbols represent the direct and indirect bandgap energies, respectively. The 10% Sn sample is located in region (iii), which is determined as a direct bandgap material. The solid and dashed lines are eye guidance of direct and indirect bandgap energies, respectively.
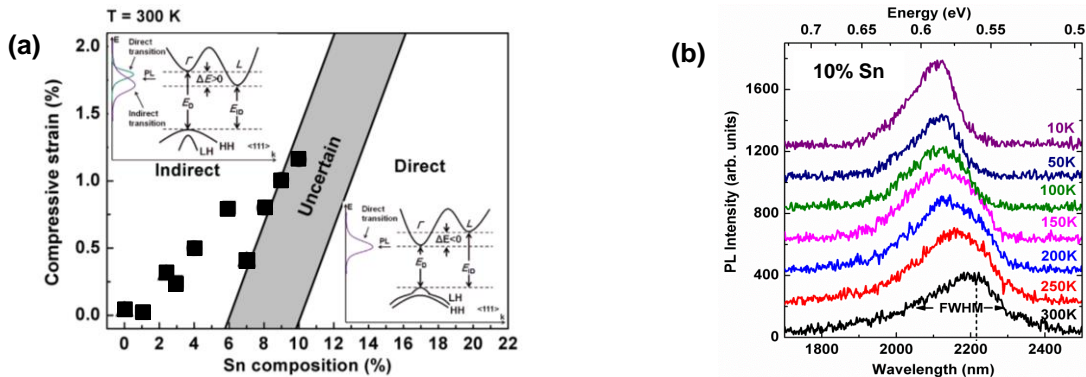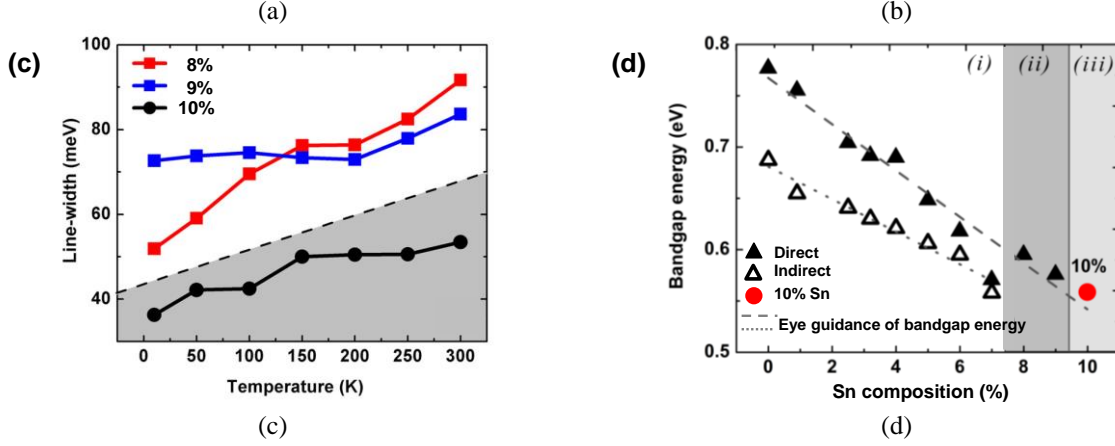
Fig. 29. (a) The effect of compressive strain and Sn composition in the indirect-to-direct bandgap transition at room temperature. (b) Temperature-dependent PL spectra of 10% Sn sample. (c) The line-width of the PL peaks as a function of temperature for samples with Sn compositions of 8, 9 and 10%. (d) Sn composition-dependent bandgap energies at room temperature.

The absorption coefficient can be used to determine the performance of photodetectors in terms of operation wavelength range, responsivity and specific detectivity; the refractive index would be very useful for the design of the anti-reflection coating for photodetectors and the layer structure for waveguides and lasers. In this project, the systematic study of the absorption coefficient and refractive index of $Ge_{1-x}Sn_x$ thin films (*x* from 0 to 10%, listed Table IV) were conducted via spectroscopic ellipsometry at room temperature.

Table IV. Summary of material characterization.

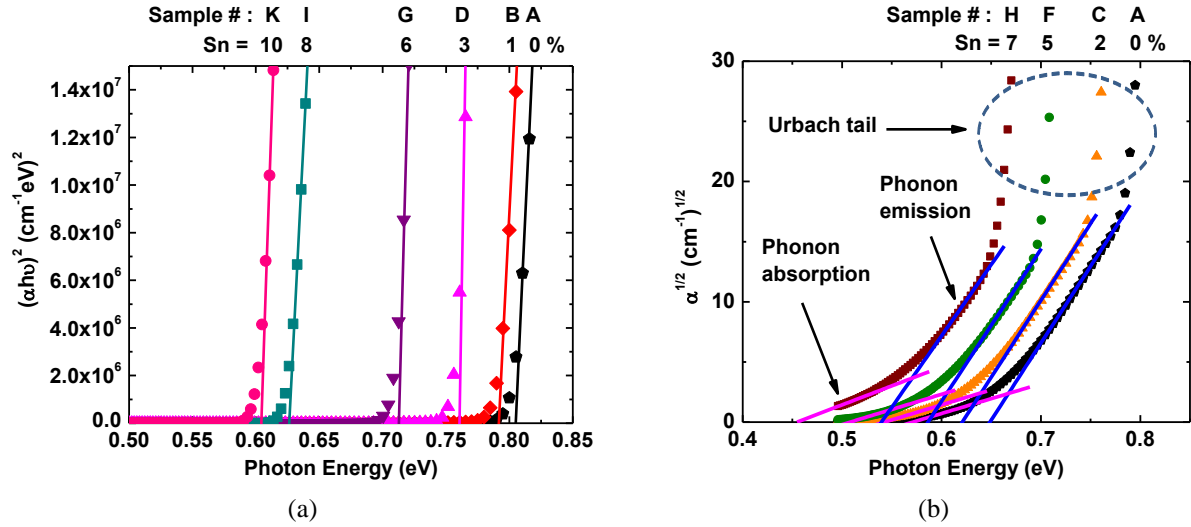| No.	Sn (%)	$Ge_{1-x}Sn_x$ film thickness (nm)	Compressive strain (in-plane, %)	E_g^{Γ} (eV)	E_g^{L} (eV)
A	0 (Ge reference)	300	0	0.805	0.610
B	1	327	0.02	0.792	0.595
C	2	40	0.22	0.772	0.582
D	3	128	0.24	0.761	0.576
E	4	70	0.50	0.723	0.574
F	5	88	0.67	0.721	0.547
G	6	96	0.82	0.713	0.534
H	7	240	0.45	0.682	0.497
I	8	90	0.80	0.626	N. A.
J	9	117	1.01	0.617	N. A.
K	10	59	1.16	0.604	N. A.

27

Fig. 30 Sn compositional-dependent absorption coefficients attributed to the (a) direct bandgap transition and (b) indirect bandgap transition. The solid symbols were obtained from the Johs-Herzinger model and the solid curves were the linear fitting. Only representative samples are shown here for clarity.

Figure 30(a) shows the Sn compositional-dependent absorption coefficient attributed to the direct transition. Some representative samples are shown here for clarity. The solid symbols were obtained from the Johs-Herzinger model and the solid curves were the linear fitting in order to extract the E_g^Γ, as summarized in Table II. As Sn composition increases, the absorption edge shifts towards lower energy, reflecting the gradually reduced bandgap as expected. It is worth pointing out that each sample in this study has different Sn composition and strain status, however, slopes of their absorption curves are mostly identical as seen in Fig. 30(a), indicating that the slope is independent of Sn composition and strain.

Figure 30(b) shows the absorption coefficient attributed to the indirect transitions in samples A-H (only samples A, C, F and H were shown for clarity). The solid symbols and curves were from the Johs-Herzinger model and linear data fitting, respectively. Two types of absorption can be clearly identified as noted in the figure, corresponding to the phonon absorption and emission processes, respectively. The extrapolations to the photon energy axis give the values of $E_g^L - h\theta$ and $E_g^L + h\theta$, with which E_g^L and phonon energy $h\theta$ were calculated. The E_g^L was listed in Table I and $h\theta$ was calculated to be 39.0±1.5 meV, consistent with reported value. For each sample, slopes of two fitted lines corresponding to phonon absorption and emission were found to be independent of the Sn composition and strain.
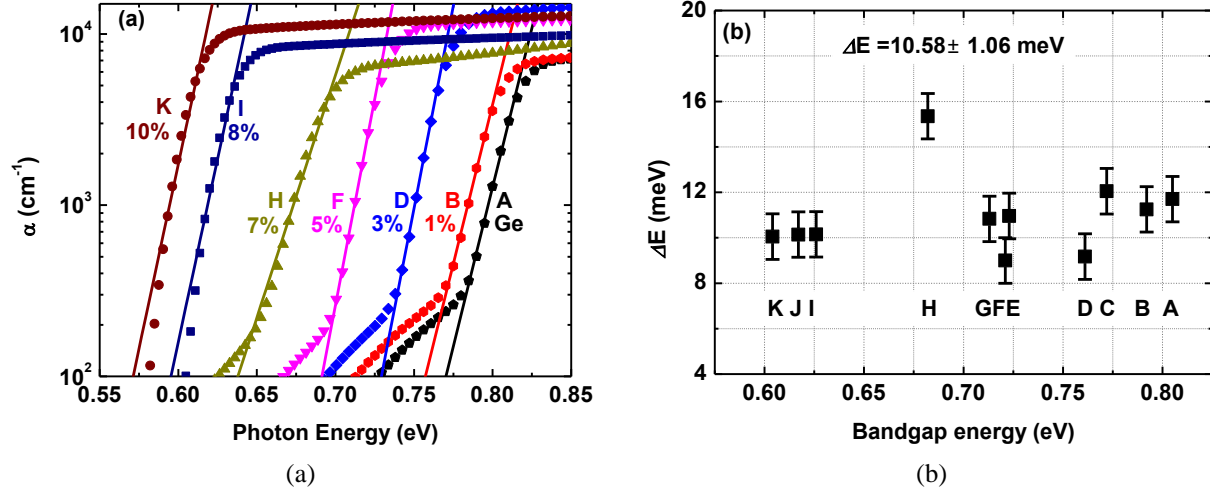
Fig. 31 (a) Urbach tail for each sample (Only selected samples were shown for clarity). The clear exponential decay of absorption coefficient as photon energy decreases was observed; (b) The Urbach parameter ΔE extracted from (a) as 10.58±1.06 meV.

The Urbach tail of each sample is shown in Fig. 31(a). Samples A, B, D, F, H, I and K were shown for clarity. The solid symbols were obtained from the Johs-Herzinger model and the solid curves were the fitting for the Urbach tail. The clear exponential decay of absorption coefficient as photon energy decreases was observed. The linear fitting between ln (α) and photon energy was used to extract the Urbach parameter ΔE. For samples A-H (Sn composition from 0 to 7%), the indirect absorption was distinctly observed at the low energy end, those data points were excluded from the data fitting. The Urbach parameter ΔE was extracted and shown in Fig. 31(b). ΔE varying from 9.00 (sample F, 5% Sn) to 12.05 eV (sample C, 2% Sn) exhibits independence of direct bandgap energy, and was calculated to be 10.58±1.06 meV. Therefore, the Urbach width ΔE is a constant or only weakly dependent on Sn composition and strain. In Fig. 31(b), the fluctuation of ΔE may be due to the non-uniformity between the samples.
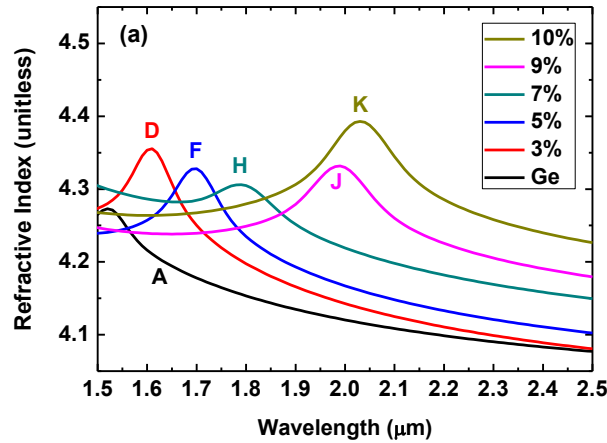

Fig. 32 Refractive index as a function of wavelength for samples A-K (only selected samples were shown for clarity). The peak in each curve is due to the Γ-valley bandgap absorption.

29

Figure 32 shows the refractive index for samples A-K (only selected samples were shown for clarity). As Sn composition increases, the refractive index increases at the same wavelength. The clear peak in each curve is related to the E_0 critical point (CP). A peak shift towards longer wavelength in E_0 CP was observed with the increase of Sn composition, which agrees well with the bandgap narrowing characteristic of $Ge_{1-x}Sn_x$ as x increases. Moreover, the absorption feature of the L-valley (the indirect bandgap) was not observed. This may be due to the weaker indirect bandgap absorption compared to the direct one.

Based on the data fitting process, the absorption coefficient formula near the bandgap was developed, as written below:

$$\alpha(h\nu) = \begin{cases} \dfrac{A(h\nu - E_g^{\Gamma})^{1/2}}{h\nu}, & (E_g^{\Gamma} + \dfrac{\Delta E}{2} \leq h\nu); \\[2em] Ae^{-1/2}(\dfrac{\Delta E}{2})^{1/2}\exp\left(\dfrac{h\nu - E_g^{\Gamma}}{\Delta E}\right) + C\left[1 - \dfrac{1}{\exp(h\theta/k_BT)-1}\right]\left[h\nu - (E_g^L + h\theta)\right]^2, & (E_g^L + h\theta \leq h\nu \leq E_g^{\Gamma} + \dfrac{\Delta E}{2}); \\[2em] B\left[\dfrac{1}{\exp(h\theta/k_BT)-1}\right]\left[h\nu - (E_g^L - h\theta)\right]^2, & (E_g^L - h\theta \leq h\nu \leq E_g^L + h\theta). \end{cases}$$

The parameters in the formula are summarized in Table V.

Table V. Summary of parameters for calculation of absorption coefficient

A ($\times 10^4$ cm^{-1}(eV)$^{1/2}$)	B ($\times 10^3$ cm^{-1}(eV)$^{-2}$)	C ($\times 10^4$ cm^{-1}(eV)$^{-2}$)	$h\theta$ (meV)	b_{GeSn}^{Γ} (eV)	b_{GeSn}^{L} (eV)	ΔE (meV)
3.68 ± 0.86	2.25 ± 0.03	2.17 ± 0.11	39.0 ± 1.5	2.92 ± 0.11	1.81 ± 0.15	10.58 ± 1.06

The refractive index formula can be written as:

$$n(\lambda) = \left[D + \dfrac{E\lambda^2}{\lambda^2 - F}\right]^{1/2} + \dfrac{\left[D + \dfrac{E\lambda^2}{\lambda^2 - F} - 1\right]\left[D + \dfrac{E\lambda^2}{\lambda^2 - F} + 2\right]}{6\left[D + \dfrac{E\lambda^2}{\lambda^2 - F}\right]^{1/2}} e_{//}$$

The expressions of parameters D, E and F are given in Table VI.

Table VI. Summary of parameters for calculation of refractive index

D	E	F (μm^2)
$(33.59 \pm 2.82)x + (14.67 \pm 0.17)$	$-(9.62 \pm 1.09)x + (1.33 \pm 0.06)$	$(21.98 \pm 2.36)x + (1.16 \pm 0.14)$

For a GeSn alloy with given Sn composition (x) and strain ($e_{//}$), the absorption coefficient near the bandgap and refractive index can be calculated.
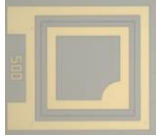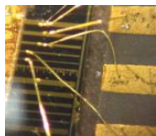
III) Fabrication and characterization of GeSn-based optoelectronic devices

GeSn samples grown by collaborator ASM have been fabricated into light emitting diodes (LEDs), avalanche photo diodes (APDs) and photodetectors. Characterization of these devices has been conducted.

GeSn mid-IR LED

On the basis of the existing Ge/GeSn/Ge DHS samples, both proof-of-concept and high power surface emitting LEDs were fabricated. In addition, the samples were also fabricated to edge-emitting devices. Both surface- and edge-emitters can be widely used for sensing applications. Table VII lists the research summary of GeSn LED.

Table VII Summary of GeSn based LED

Type of LED device		Top view of device image	Sn compositions: 6, 8, 9, 10%
			Specifications
Surface emitting LED	1st generation		• For baseline study, material quality evaluation; • Device sizes from 0.5 to 2mm in side length.
	2nd generation		• For in-depth study. Extended metal pads for wire bonding; • High power emission; • Device sizes from 50 to 250μm in radius.
	3rd generation		• Fishnet top contact design for uniform current flow; • High power emission; • Device sizes from 0.5 to 2mm in side length.
Edge emitting LED			• Pioneer study of group IV based electrical injection laser; • Light source for On-chip integration sensing system applications; • Device sizes from 80 to 120μm in cavity width, and 500~800 μm in cavity length.

1st generation LED: Fig. 33(a) shows the normalized EL spectra for 1st generation surface emitting LEDs at room temperature. As Sn composition increases, the EL peak position shifts to longer wavelength. The EL emission at 2380 nm was observed from 10% Sn LED. For the devices with 9 and 10% Sn LEDs the PbS detector (cut-off at 3 μm) is applied to measure the spectra, whose signal-to-noise ratio is lower than that of the InGaAs detector (cut-off at 2.3 μm) which is used to measure the EL of LEDs with 6 and 8% Sn LEDs.
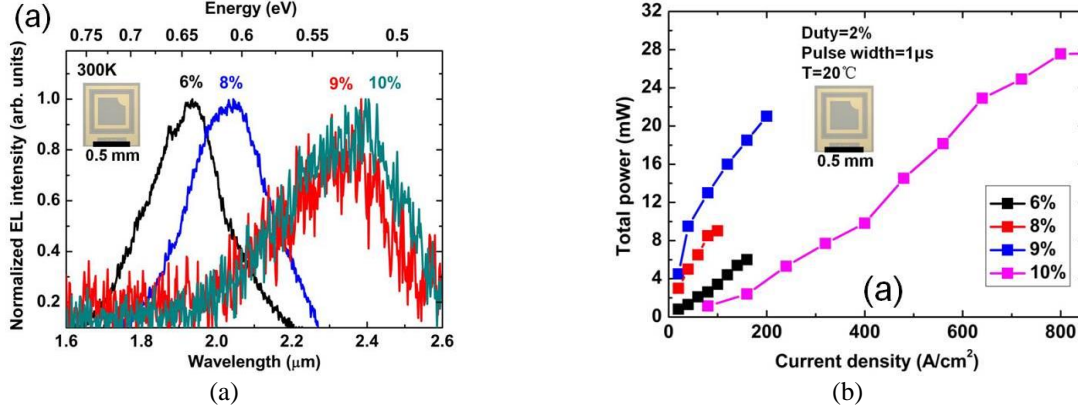
Fig. 33. (a) Normalized EL spectra of 1st generation LEDs at 300 K. (b) The peak emission power of 6, 8, 9 and 10% Sn LED at 20 ^{0}C.

The emission power measurement has been performed by using a pulsed current source in order to eliminate the contribution from Joule heating. Figure 33(b) shows the peak emission power for 6, 8, 9 and 10% Sn 1st generation LEDs (0.5 mm square mesa device) at 20 ^{o}C. With a 2% duty cycle and 1 μs pulse width of current source, the maximum peak power of ~28 mW at 800 A/cm^2 has been obtained from a 10% Sn LED.
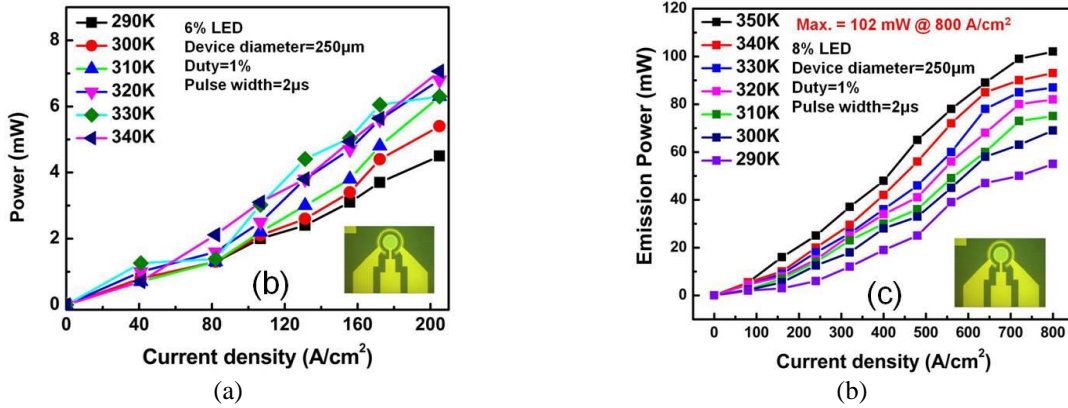

Fig. 34. The peak emission power of (b) 6% Sn and (c) 8% Sn 2nd generation LED under different current injection at temperatures from 290 to 340 K.

2nd generation LED: The 2nd LEDs show similar Sn composition dependent spectra behavior. Temperature-dependent power measurement has been conducted for 6 and 8% Sn LEDs with 250 μm in device diameter from 290 to 350 K, as shown in Fig. 34. Current with 1% duty cycle and 2 μs pulse width was applied. As temperature increases, the peak emission power increases under the same current injection level. This is due to the more injected carriers populate the Γ valley with increased temperature, therefore the radiative recombination was enhanced, resulting in the increased emission power. The peak emission power of 0.1 W has been achieved for an 8% Sn LED at an injection of 800 A/cm^2 and a working temperature of 350 K, as shown in Fig. 34(b).
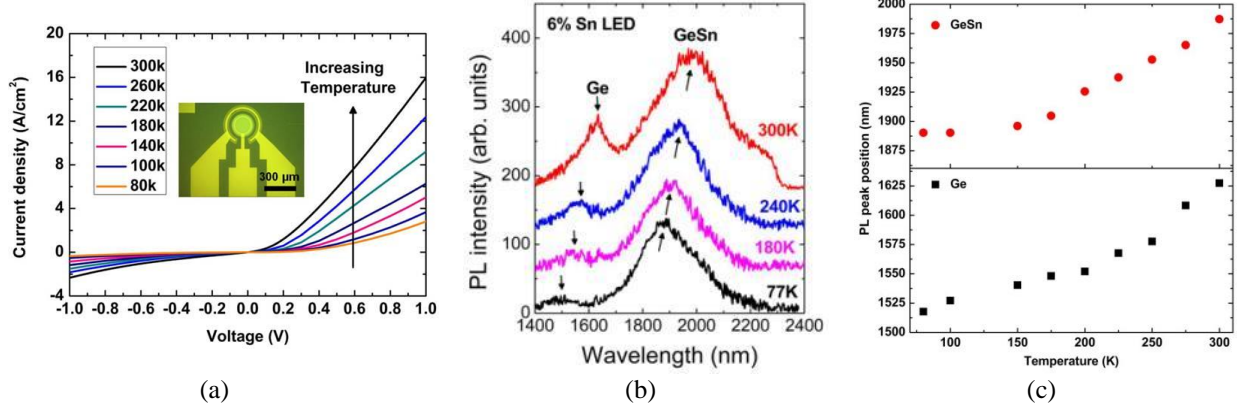
Fig. 35. Characteristics of 2nd generation 6% Sn LED. (a) The temperature-dependent I-V characteristic. Inset: Optical image top view image of the device. (b) The temperature-dependent EL emission spectra (c) Peak position as function of temperature extracted from (b).

The temperature-dependent behaviors of 2nd generation Ge$_{0.94}$Sn$_{0.06}$ LEDs have been investigated at temperatures from 80 to 300 K. The current-voltage characteristic and optical image top view of the device are shown in Fig. 35(a). The clearly rectifying behavior is observed at temperatures from 80 to 300 K. The decrease in device resistance by increasing the temperature is due to the increasing number of activated carriers in the device. Figure 35(b) shows the temperature-dependent EL spectra of Ge$_{0.94}$Sn$_{0.06}$ LED from 80 to 300 K at an injection level of 600 A/cm^2. The peak shift to shorter wavelength at lower temperature is observed, which is consistent well with Varshni's relation: $E_g(T) = E_g(0) - \frac{\alpha T^2}{T+\beta}$, where $E_g(0)$ is the bandgap energy of Ge$_{0.94}$Sn$_{0.06}$ at zero K, T is temperature, and α and β are fitting parameters. Based on the $E_g(0) = 0.63\ eV$ and the peak position varying from 1980 nm at 300 K to 1900 nm at 80 K, the α and β are fitted as 3.2×10^{-4} eV/K and 275 K, respectively, which agrees with previous study on temperature-dependent PL spectra of 6% Sn sample. A small peak at around 1550 nm in most EL spectra is attributed to EL from the Ge layer, whose direct bandgap energy is 0.8 eV at room temperature. The EL peak position as function of temperature is summarized in Fig. 35(c).
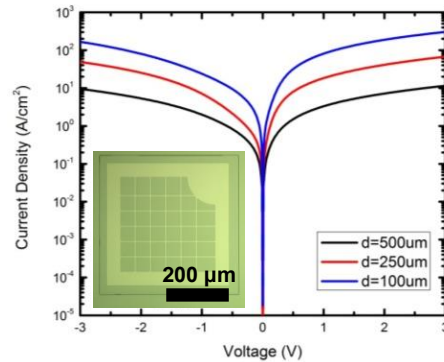

Fig. 36. Current-voltage curves of 10% Sn 3rd generation LED with fishnet top contact structures.

3rd generation LED: For the 3rd generation LED, the fishnet structure is used for top contact in order to improve the uniformity of current injection. Moreover, the high power emission can be

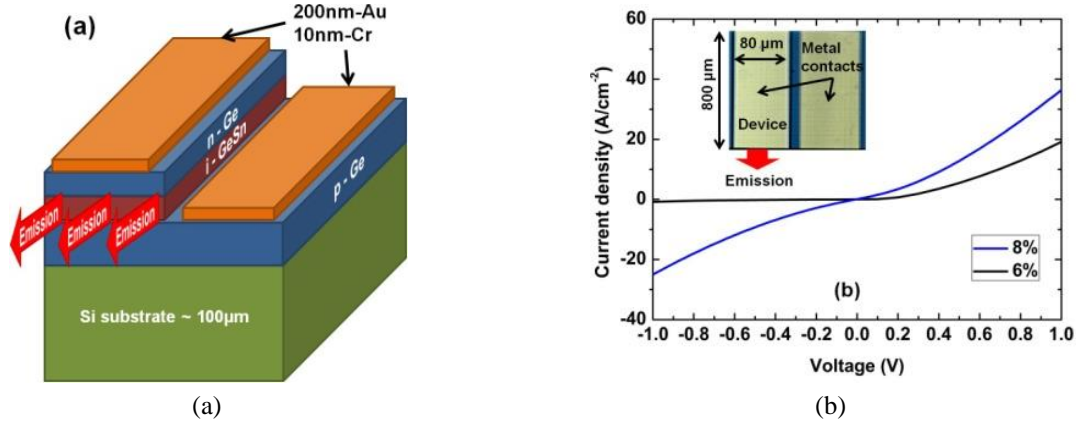expected with larger active area of emitter. The preliminary current-voltage results are shown in Fig. 36.

(a)   (b)

Fig. 37. (a) Schematic of the device; (b) I-V characteristics. The inset shows top view image of the device.

Edge emitting LED: The samples were also fabricated to edge-emitting devices. Figure 37(a) shows the schematic drawing of the device. The current-voltage characteristic and optical image top view of the device are shown in Fig. 37(b) (W=80 μm, L=800 μm). The clearly rectifying behavior is observed, indicating the good Ohmic contact. As Sn composition increases, the current density increases under the same forward voltage due to the narrowed bandgap with higher Sn composition.

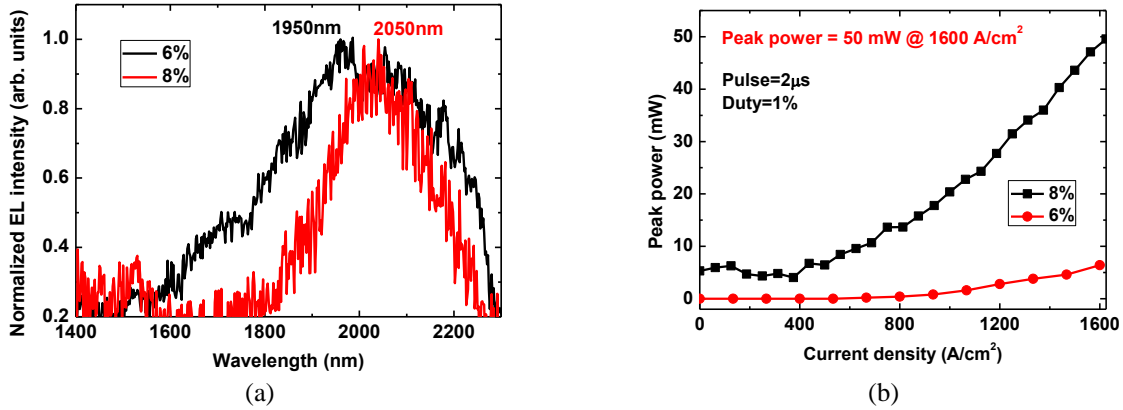(a)   (b)

Fig. 38. (a) Room temperature EL spectra of 6 and 8% Sn edge emitting LEDs; (b) Peak emission powers of 6 and 8% Sn LEDs at room temperature.

Figure 38(a) shows normalized EL spectra of 6 and 8% Sn LEDs at room temperature. As the Sn composition increases, the EL peak shifts towards longer wavelength due to the reduced bandgap energies. The EL emission at 1950 and 2050 nm were observed from 6 and 8% Sn LEDs, respectively. These results are consistent with surface emitting LED. Figure 38(b) shows the peak emission power as a function of current injection densities at room temperature. For each LED, the emission power increases as current increases. A saturation power was observed at 1600 A/cm^2, which is due to the voltage compliance of the current source. As Sn composition increases, the peak power increases under same current injection. The peak emission power of 50 mW has been achieved for an 8% Sn edge emitting LED at an injection of 1600 A/cm^2.

Avalanche photo diode

Avalanche photo diode (APD) based on Separate Absorption-Charge-Multiplication (SACM) structure has been fabicated. The design (shown in Fig. 39(a)) takes advantage of the excellent optical absorption of GeSn at mid-IR range and the outstanding carrier multiplication properties of Si. In the high-electric-field gain region of Si, photogenerated electrons from the GeSn absorption layer undergo a series of impact ionization processes, which consequently amplifies the photocurrent and improves the sensitivity. Figure 39(b) shows a schematic of the cross-section for the APD device. Due to the current growth limitation, GeSn layer (7% Sn) was grown on a thick Ge buffer layer not directly on Si. The preliminary testing results of the temperature dependent I-V curves have shown device breakdown behavior in Fig. 39(c). However, the device spectrum response does not show any IR response due to GeSn or Ge absorption. It is believed that the conduction band discontinuity might be the reason to stop electron propagating to Si for avalanche process. A possible solution is to engineer the local doping profile so that the electron could be easily collected.
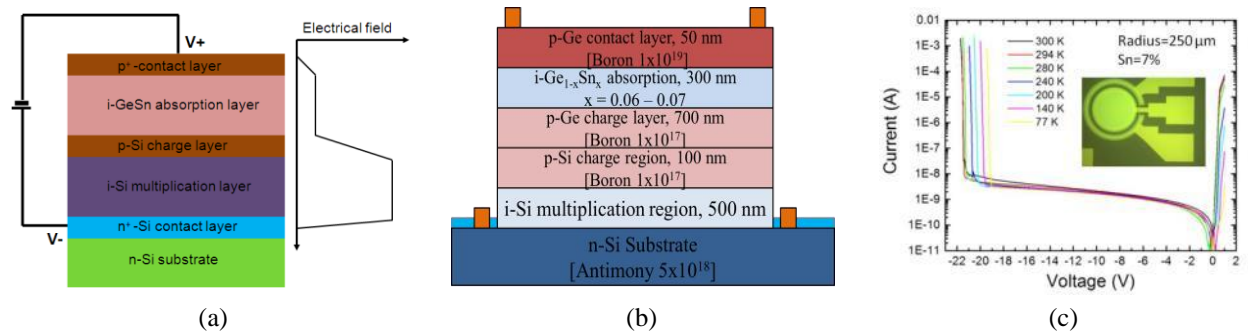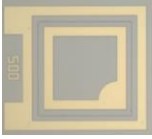

| (a) | (b) | (c) |

Fig. 39 (a) Schematic cross-section of a GeSn/Si APD with a SACM structure and its internal electric field distribution. (b) Structure of GeSn avalanche photo diode (APD) with a SACM structure. (c) Temperature dependent I-V of 7% Sn APD indicates the breakdown voltage. Inset: Optical image of the device.

GeSn photodetectors

By leveraging the high quality GeSn material growth capability, we have developed a set of processes for different photo detectors. In-depth of study has been conducted for GeSn photo conductors and photodiodes. A summary of the photo detector work is given in Table VIII.

Table VIII Summary of photo detector devices

Type of photo detector	Top view of device image	Sn composition	Specifications
Standard Photoconductor		1-10%	• GeSn bulk samples; • For baseline study of photo response, carrier lifetime and material quality evaluation.
Interdigitated photoconductor		1-10%	• GeSn bulk samples; • Newly designed high gain photoconductor; • Interdigitated electrodes with spacing of 6, 12 and 24μm;

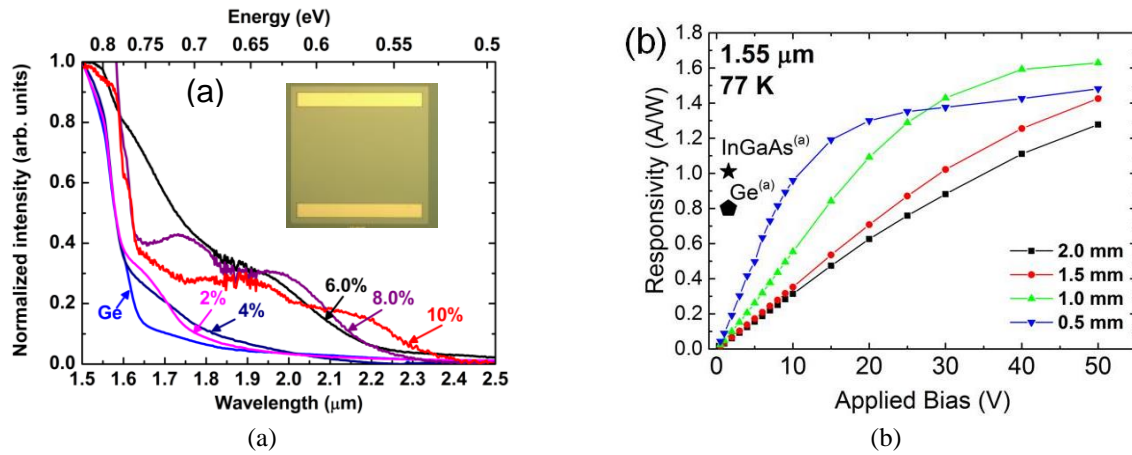|			
			• Effective carrier lifetime evaluation; • Capability of high speed operating measurement.
1st Generation Photo diode		6, 8, 9, 10%	• Ge/GeSn/Ge n-i-p DHS; • Low dark current; • Low voltage operation.
2nd Generation Photo diode		7, 9, 10%	• Reduced device size for uniform current; • Detailed current-voltage, responsivity and specific detectivity (D*) study.

Fig. 40. (a) Room temperature spectral photo response of standard photoconductors with Sn compositions up to 10 %. (b) Responsivity measured at 77 K for each mesa size of $Ge_{0.9}Sn_{0.1}$ photoconductor. Representative responsivities of InGaAs and Ge detectors are given for comparison.

Standard Photoconductors: Room temperature spectral photo response of standard photoconductors has been measured as shown in Fig. 40(a). As Sn composition increases, the cutoff wavelength shifts towards to longer wavelength and the longest cutoff wavelength of 2.4 μm is observed for a 10 % Sn device. Temperature dependent responsivity for different device sizes and bias voltages are conducted thoroughly. Typical $Ge_{0.9}Sn_{0.1}$ photoconductor responsivity result measured at 1.55 μm under 77 K is shown in Fig. 40(b). The saturation of the responsivity is due to the carrier sweep-out effect. The peak responsivity value of 1.63 A/W measured at 77 K, was observed at 50 V bias on a 1 mm mesa device. At 77 K, the responsivity of $Ge_{0.9}Sn_{0.1}$ photoconductors exceeds that of commercially available InGaAs and Ge photovoltaic detectors at 1.55 μm.
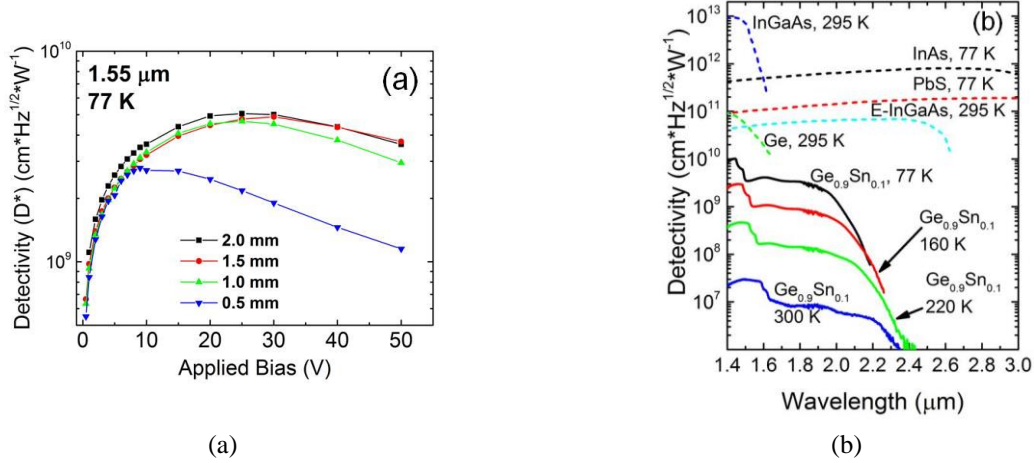
(a)

(b)

Fig. 41. (a) D* measured for 77 K at a 1.55 μm wavelength. Measurements were conducted on each mesa size as a function of the applied voltage bias. (b) D* for 300, 220, 160, and 77 K were measured with a 10 volt DC bias across the 2.0 mm mesa device. D* for other detectors in the same spectral range are plotted for comparison.

Using the 1 Hz equivalent noise bandwidth of the measurement setup, the known device area, and the calculated noise current, the D* in Fig. 41(a) is calculated based on the measured AC responsivity values from Fig. 40(b). The responsivity saturates at high voltage, while the noise component increases as $V^{1/2}$ leading to the overall decreasing D* for further increased bias. The peak D* value 5×10^9 cm*Hz$^{1/2}$*W^{-1} of the 2.0 mm detector occurs at an applied bias of 25 V, followed by a decrease in D* for further increasing bias. The spectral D* in Fig. 41(b) for different temperatures shows the comparison of these devices with other mature detector technologies. Note that the D* of Ge$_{0.9}$Sn$_{0.1}$ is only one order-of-magnitude lower than that of Ge, extended-InGaAs, and PbS detectors in the short wavelength IR range. A reduction of the device dark current through thicker active layers and a decrease of the dominant noise by reducing defects at the growth interface would dramatically improve the D* for these types of Ge$_{1-x}$Sn$_x$ detectors, making their performance superior to the commercially available IR detectors in the same wavelength range.
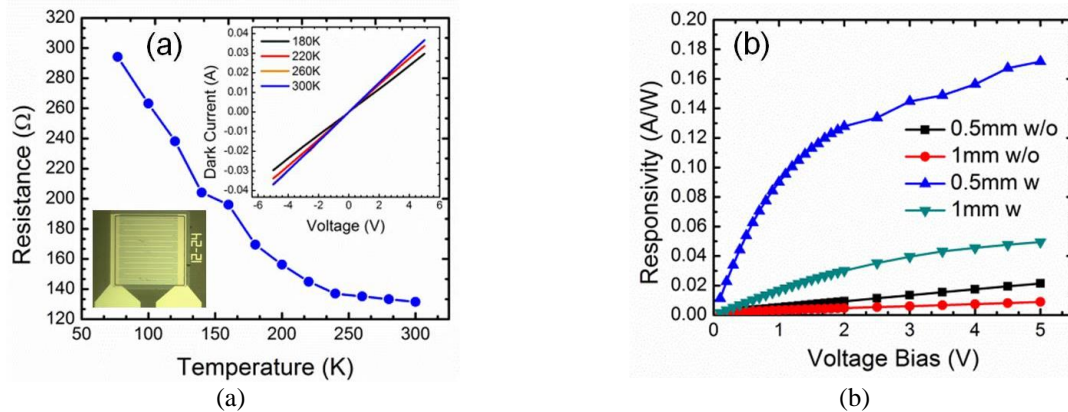

(a)

(b)

Fig. 42. (a) The dark resistance of the 0.5 mm mesa device. Insets: Optical image top view of the device and linear behavior of dark I-V indicates good Ohmic contact. (b) Comparison of responsivities between the devices with and without interdigitated electrodes.

Photoconductor with interdigitated electrodes: In order to obtain a high gain photoconductor, a newly designed photoconductor with interdigitated electrodes has been fabricated and characterized. Figure 42(a) plots the resistance value extracted from the dark I-V measurement at temperatures from 300 to 77 K. The linear I-V shown in the inset indicates good Ohmic contact. As the temperature decreases, the resistance increases as a result of the decreasing number of activated carriers in the device. The responsivities of the $Ge_{0.9}Sn_{0.1}$ photoconductor with and without interdigitated electrodes at room temperature are shown in Fig. 42(b). The newly designed interdigitated photoconductor allows an enhancement factor of 8 for the 0.5 mm mesa device and 5.6 for the 1 mm mesa device under 5 V bias, respectively.
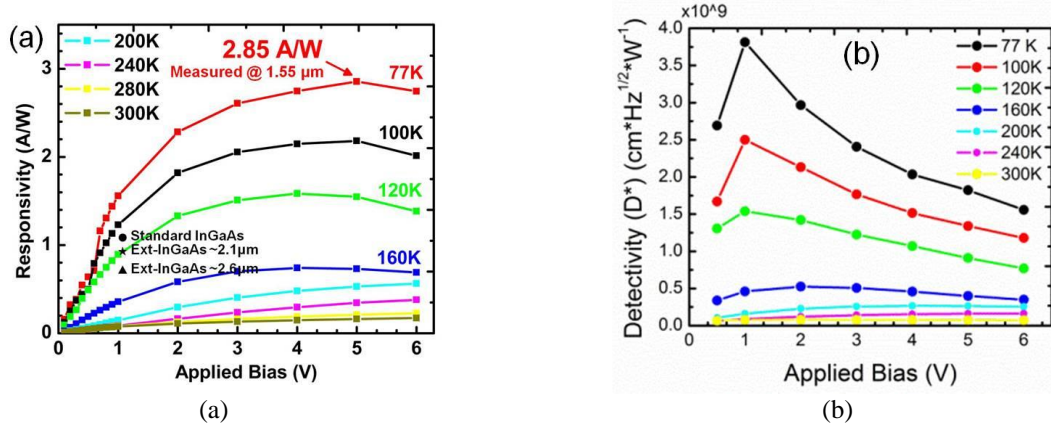

Fig. 43. (a) Responsivity measured for the 0.5 mm mesa device at temperatures from 300 to 77 K. Responsivities for other detectors at 1.55 μm are plotted for comparison. (b) D* of the 0.5 mm mesa device at temperatures from 300 to 77 K.

Figure 43(a) shows a clear enhancement of responsivity with decreasing temperature for the 0.5 mm mesa device. A maximum responsivity of 2.85 A/W under 5 V bias at 77 K was achieved, which is three times of commercially available InGaAs and Ge photovoltaic detectors at 1.55 μm. As temperature decreases, the activated background carrier concentration is reduced while the effective carrier lifetime increases, resulting in the improvement of the responsivity at low temperature. The D* was consequently calculated based on measured responsivity at different temperatures, as shown in Fig. 43(b). For this set of devices wherein the dark current is high, the shot noise dominates over other noise mechanisms. As applied voltage increases, the noise current increases proportionally with $V^{1/2}$ while the responsivity saturates. Therefore, the D* decreases after a certain applied voltage. At 77 K, the peak D* value of 3.81×10^9 $cm*Hz^{1/2}*W^{-1}$ was observed at 1 V. The D* can be improved by optimizing the geometry parameters of interdigitated electrodes to allow high responsivity and low noise current.

A 500-nm-thick $Ge_{0.93}Sn_{0.07}$ layer was grown on top of a Ge buffered Si substrate. The sample was then fabricated into metal-semiconductor-metal devices (500×500 μm^2) using standard lithography and wet etch processes. In order to enhance the photoconductive gain, the interdigitated electrodes consist of 10 nm Cr and 150 nm Au were patterned with the fingers width of 3, 6 and 12 μm and corresponding spacing between fingers of 6, 12 and 24 μm, respectively (annotate as 3-6, 6-12 and 12-24 hereafter). Temperature dependent study has been performed by using a LN$_2$-cooled Janis cryostat.
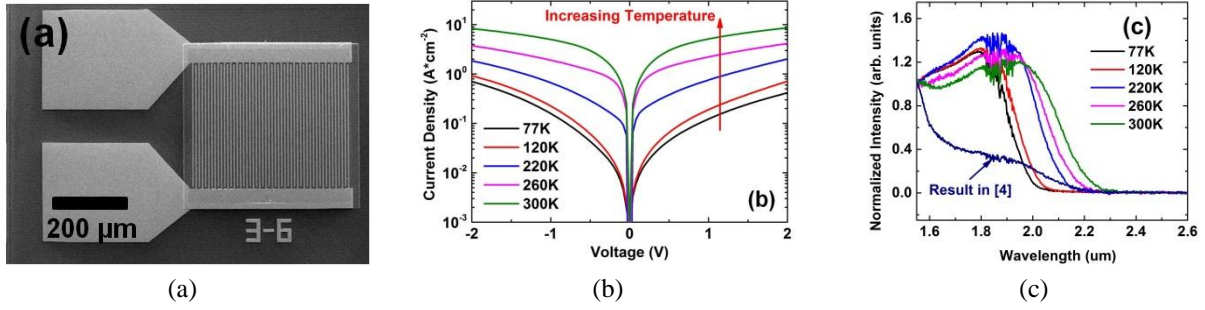
Fig. 44. (a) SEM image top view of the 3-6 device; (b) Dark current-voltage characteristics at the temperatures from 300 to 77K; (c) Temperature-dependent spectral response. The previous result for GeSn photoconductor with thin film GeSn (<200 nm) is also plotted for comparison.

Fig.(a) and (b) show the top view scanning electron microscope (SEM) image of the 3-6 device and the typical dark current-voltage characteristics at the temperatures from 300 to 77 K. As the temperature increases, the dark current increases as a result of the more thermal activated carriers. The temperature-dependent spectral response is shown in Fig.(c). The cut-off wavelength of 2.4 µm was observed at 300 K. Compared to our previous study on thin film (less than 200 nm) $Ge_{0.93}Sn_{0.07}$ photoconductor, the photo response signal is significantly enhanced, indicating the improved material quality. Moreover, the cut-off wavelength shifts towards longer wavelength. This can be explained as the thicker GeSn layer relaxes the material, which narrows the bandgap of GeSn, resulting in the extended spectral response.
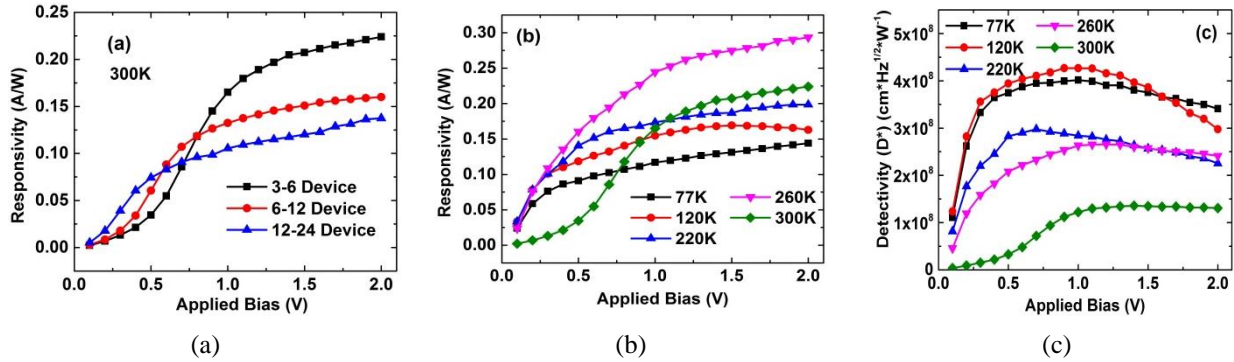
Fig.45. (a) Responsivity for different devices; (b) Responsivity of 3-6 device at the temperatures from 300 to 77 K; (c) D* of 3-6 device at the temperatures from 300 to 77 K.

Fig.(a) shows the responsivity of 3-6, 6-12 and 12-24 devices at 300 K, respectively. Since the photoconductive gain is reverse proportional to the carrier transit time, the responsivity increases as the spacing between the electrodes reduces, as shown in Fig. 45(a). For each device, as the applied bias increases the responsivity increases. The saturation behavior was observed at around 1 V. This behavior in the photoconductive gain is due to the minority carrier sweep-out effect. The temperature-dependent responsivity of 3-6 device is plotted in Fig.(b). As the temperature decreases, the carrier lifetime increases due to the reduced concentration of scattering centers in the material, therefore more photo generated carriers can be collected before their recombination, resulting in the enhanced photoconductive gain and responsivity. However, the peak responsivity of 3-6 device was obtained as 0.29 A/W at 2 V bias and 260 K. This is due

to the increases bandgap of GeSn at lower temperature, which changes the absorption coefficient.

The D* was consequently calculated based on the measured responsivity and the calculated noise at different temperatures, as shown in Fig. 45(c). The thermal noise and shot noise are dominant based on our investigation. As the temperature increases, both noises increase. The peak D^* of 4.27×10^8 cm*Hz$^{1/2}$*W^{-1} was observed at 0.9 V and 120 K. As the applied voltage increases, the noise current increases by a factor of $\sqrt{V}$ while the responsivity saturates. Therefore, the D* decreases after a certain applied voltage.
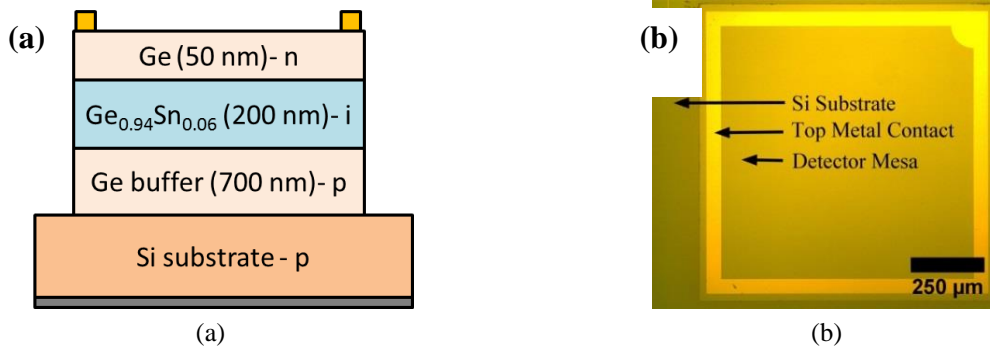
Fig. 46. (a) Cross section view and (b) top down view of the fabricated Ge$_{0.94}$Sn$_{0.06}$ p-i-n photodiode.

1st generation photodiode: The photodiode mesa was patterned with standard photolithography and etched down to the Si substrate. Square photodiode mesas of 2 x 2 mm and 1 x 1 mm were fabricated and tested. The metal contacts of Al and Au/Cr were used for the Ohmic contacts on the Si backside and top Ge cap layer, respectively. The cross section in Fig. 46(a) shows the fabricated detector structure. A top view optical image of the 1 mm square photodiode in Fig. 46(b) shows the top contact layout.
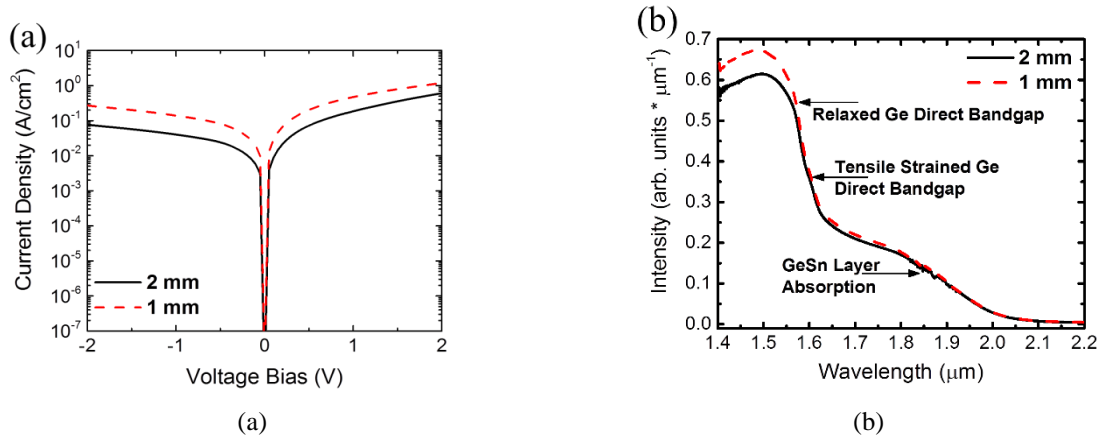
Fig. 47. (a) Dark current density of the p-i-n Ge$_{0.96}$Sn$_{0.04}$ measured for a 1 and 2 mm mesa. (b) Spectral response of the photodiode shows photo response out to 2.0 μm.

The I-V relationship of the devices in Fig. 47(a) shows the rectifying behavior of these devices. The large reverse current may result from the narrowed bandgap and the defects located at the

Ge/GeSn interface. The spectral response of the photodiodes presented in Fig. 47(b) show the strong absorption starting at 1.55 μm due to the relaxed Ge buffer layer. A shoulder feature at 1.6 μm is also observed and is attributed to the tensile strain induced red-shift of the band edge for the Ge cap layer. The falling edge of $Ge_{0.94}Sn_{0.06}$ absorption begins at 1.8 μm and the 50 % cut-off occurs at 1.92 μm. The absorption band edge is around 2.05 μm which corresponds to an energy of 0.605 eV. Based on a Vegard's law calculation with bowing parameters for the $Ge_{0.94}Sn_{0.06}$ Γ-valley at room temperature, the expected band gap for a relaxed film is 0.587 eV. The difference is attributed to the compressive strain in the active $Ge_{0.94}Sn_{0.06}$ layer that raises the conduction band edge.

(a)   (b)
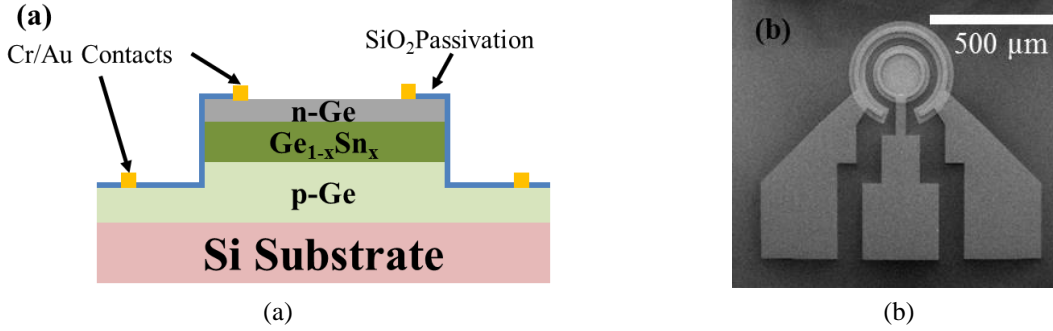
Fig. 48. (a) Schematic cross-sectional view of the device structure. (b) Top view SEM image of 250 μm device.

2nd generation photodiode: GeSn DHS photodiode samples were fabricated with a structure composed of a 50-nm-thick n-type Ge cap layer, a 200-nm-thick GeSn active layer, and a 750-nm-thick p-type Ge layer (also serving as buffer layer). Since the doping concentration of the unintentionally doped active layer was measured as 1×10^{17} cm^{-3} (p-type), the p-type and n-type Ge layers were therefore doped at 5×10^{18} and 1×10^{19} cm^{-3} to form a good p-n junction. The circular mesas with 250 and 500 μm diameters were fabricated by using standard photolithography and wet etching processes. A 10/200 nm Cr/Au bilayer was deposited to form metal contacts. The schematic cross sectional view and the top view SEM image of the device is shown in Fig. 48.

(a)   (b)

Fig. 49. Temperature dependent I-V characteristic of GeSn photodiode with (a) 7 % Sn and (b) 10 % Sn. The mesa size is 250 μm in diameter.

Figures 49(a) and 3(b) show the dark current-voltage (I-V) characteristics from 300 to 77 K of the GeSn photodiodes (mesa size of 250 µm in diameter) with Sn compositions of 7 and 10 %, respectively. The rectifying diode like behavior was observed on both devices at each temperature. As the temperature increases, the reverse current density increases as a result of more thermally activa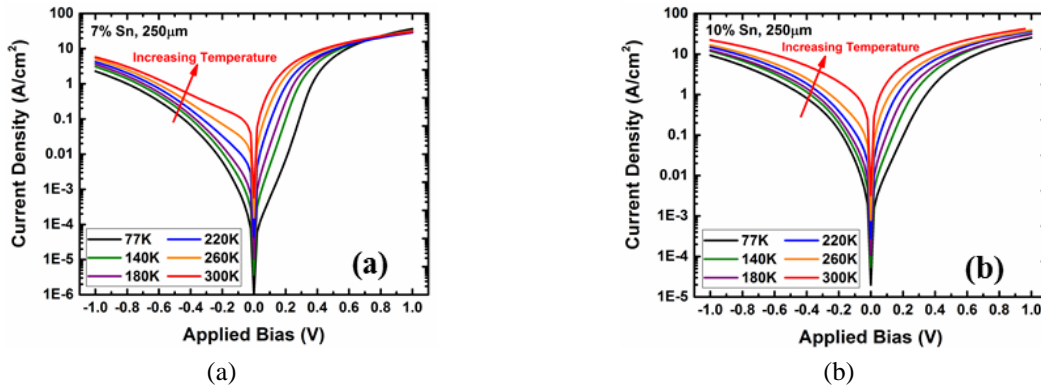ted carriers. At a certain reverse voltage, the current density of the 10 % Sn device is higher than that of the 7 % Sn device for each temperature. This is mainly due to the narrower bandgap of the 10 % Sn device compared to that of the 7 % Sn device due to the higher Sn composition, which results in the more thermally excited carriers.

The series resistance, shunt resistance, reverse saturation current, and activation energy at 77 and 300 K have been extracted by fitting the I-V curves in Fig. 15, as summarized in Table IX.

Table IX. Series Resistance, Shunt Resistance, Reverse Saturation Current, and Activation Energy at 77 and 300 K

Device	77 K			300 K			E_A (eV)
	R_S (Ω)	R_{Sh} (kΩ)	I_0 (A)	R_S (Ω)	R_{Sh} (kΩ)	I_0 (A)	
7 % Sn, 250 µm	26.2	599	6.4×10^{-8}	55.5	0.85	2.2×10^{-5}	0.14
7 % Sn, 500 µm	19.6	101	2.4×10^{-7}	44.7	0.22	5.9×10^{-5}	0.13
10 % Sn, 250 µm	35.6	23.0	3.2×10^{-6}	40.6	0.21	6.9×10^{-5}	0.13
10 % Sn, 500 µm	33.2	4.70	2.6×10^{-5}	41.3	0.08	8.1×10^{-5}	0.10

As the Sn composition increases, the shunt resistance R_{sh} decreases while the reverse saturation current I_0 increases. On the other hand, devices with larger mesa size feature lower shunt resistance and higher saturation current compared to those with smaller mesa size. There is no clear trend for the series resistance Rs, which ranges from 19.6 Ω (7 % Sn, 500 µm) to 35.6 Ω (10 % Sn, 250 µm) at 77 K and from 40.6 Ω (10 % Sn, 250 µm) to 55.5 Ω (7 % Sn, 250 µm) at 300 K. It is desirable to have small series resistance in a photodiode. For our samples, the high series resistance might be attributed to the relatively thin n-type Ge contact layer (50 nm cap layer). In contrast with R_S, infinite parallel shunt resistance R_{sh} is desirable in a photodiode since it reduces the thermal noise effect. A parallel shunt resistance from 100 to 600 kΩ and 5 to 23 kΩ at 77 K and from 220 to 850 Ω and 84 to 214 Ω at 300 K was obtained for 7 and 10 % Sn devices, respectively. The lower value of shunt resistance with the higher Sn-composition device signals the existence of the leakage current. The device with larger perimeter featuring lower shunt resistance was observed as expected. From the temperature-dependent reverse saturation current, the Arrhenius activation energies E_A for both devices were extracted. According to the theoretical study, the $E_A \sim E_g/2$ indicates that the Shockley-Hall-Read recombination is the main source of dark current. For the E_A obtained in this study, their values ranging from 0.1 to 0.14 eV were much lower than $E_g/2$ (~0.28 and 0.24 eV for 7 and 10 % Sn devices, respectively), which seems to suggest a process of defect-assisted tunneling and/or thermionic tunneling. The reverse dark current density was further investigated to estimate the surface leakage current, which is proportional to the perimeter of the device under test. At -1 V, J_{surf} were extracted to be ~ 2

mA/cm and 40 mA/cm for 7 and 10 % Sn sample at 77 K, respectively. As the temperature increases to 300 K, these values reach 18 mA/cm and 100 mA/cm.

(a)   (b)
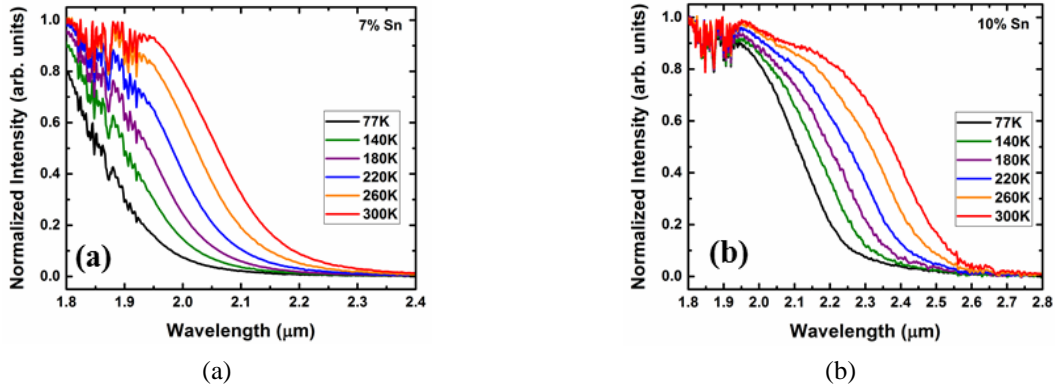
Fig. 50. Temperature dependent spectral response of (a) 7 % and (b) 10 % Sn photodiode.

Figures 50(a) and (b) show the spectral response of 7 and 10 % Sn photodiode detectors in the temperature range from 300 to 77 K. The red shift of absorption edge as the temperature increases was observed for both devices. The 7 % Sn device exhibits a cutoff wavelength of 2.0 and 2.2 μm at 77 and 300 K, respectively. Such cutoff wavelengths are way beyond the Ge band-to-band absorption edge (1.55 μm), indicating that the photoresponse beyond 1.55 μm is mainly contributed by the GeSn absorption. For the 10 % Sn device, the observed photoresponse extended to 2.3 and 2.6 μm at 77 K and 300 K, respectively. This longer wavelength coverage is due to the reduced bandgap for the increased Sn composition as expected by Vegard's law interpolation of Ge and Sn. The signal distortion at 1.8-1.9 μm is due to the atmospheric absorption that occurred for all of devices regardless of the Sn composition and temperature.

(a)   (b)
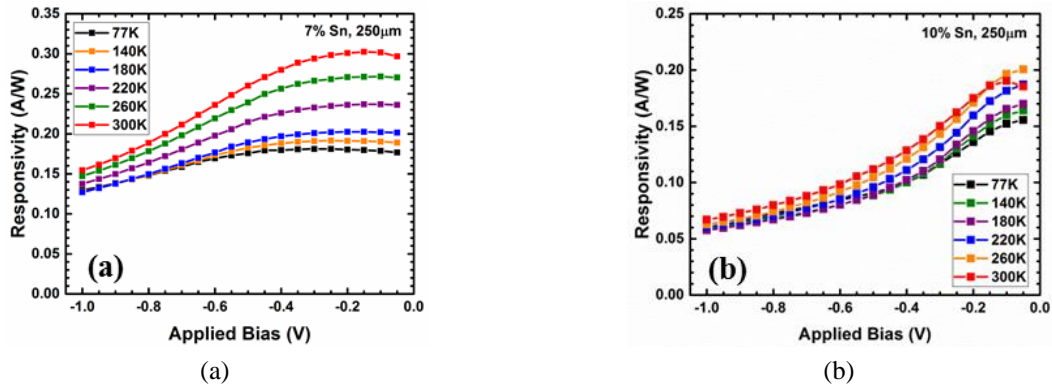
Fig. 51. Temperature dependent responsivity measured at 1.55 μm of (a) 7 % Sn and (b) 10 % Sn devices with mesa size of 250 μm in diameter.

Figures 51(a) and (b) show the responsivity at 1.55 μm of 7 and 10 % Sn photodiode devices at the temperatures ranging from 77 to 300 K. The peak responsivities of 0.3 and 0.19 A/W were obtained at 300 K with 0.1 V reverse bias voltage for 7 and 10 % Sn samples respectively. As the reverse bias voltage increases, the responsivity decreases. This may be due to the higher leakage current under higher reverse bias voltage. In addition, it has been reported that the voltage dependent change of absorption coefficient as a result of the Franz-Keldysh effect could

43

affect the responsivity. At 1 V reverse bias voltage, the responsivities reduce to 0.15 and 0.07 A/W for 7 and 10 % Sn devices, respectively. The temperature dependent responsivity shows the monotonically decreased value at lower temperatures for both devices. The increasing bandgap with the decreasing temperature is responsible for this with the absorption coefficient drop. Moreover, in general the responsivity of the 7 % Sn sample is higher than that of the 10 % Sn sample. This is mainly due to the higher material quality of the 7 % Sn sample, which was confirmed by the material characterization. The lower material quality of the 10 % Sn sample leads to the enhanced non-radiative recombination such as Shockley-Read-Hall recombination (recombination through the defect levels), which reduces the extraction efficiency of photo generated carriers, resulting in lower responsivity.

(a)   (b)
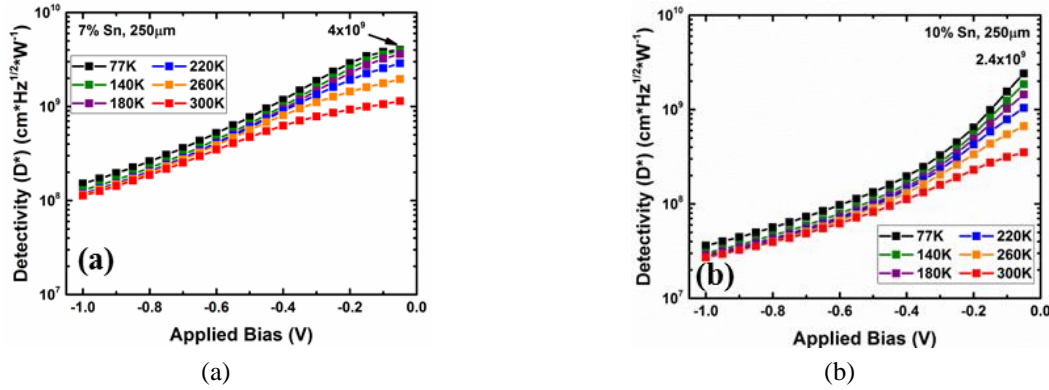
Fig. 52. Temperature-dependent D* of (a) 7 % Sn and (b) 10 % Sn device with mesa size of 250 μm in diameter.

Figures 52(a) and (b) show the D* of 7 and 10 % Sn devices with a diameter of 250 μm from 77 K to 300 K. The peak D* of 4×10^9 and 2.4×10^9 cmHz$^{1/2}$W^{-1} for 7 and 10 % Sn devices were obtained at 77 K, respectively. Although the responsivity exhibits the smallest value at this temperature, the dark current significantly decreases, resulting in the improved D* value compared to that at 300 K. The lower peak D* of the 10 % Sn device compared to that of the 7 % Sn device is due to the smaller responsivity and larger noise power. Moreover, the D* of devices with different mesa sizes show the very close values under the same temperature and bias voltage, suggesting the uniform device quality of $Ge_{1-x}Sn_x$ detectors.

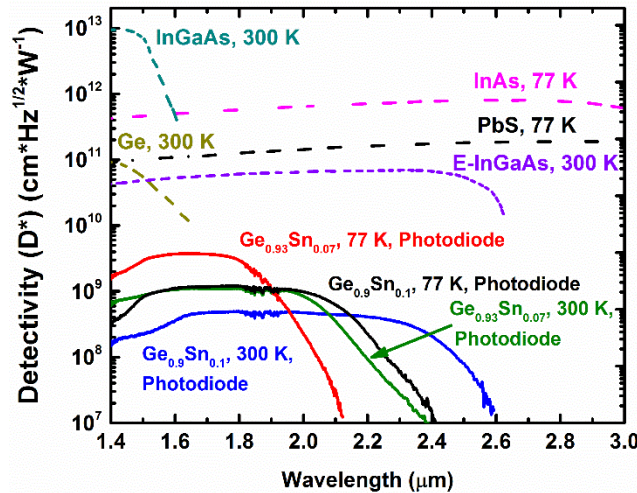Fig. 53. Spectral D* of 7 and 10 % Sn photodiodes measured at 0.1 V reverse bias voltage across a 250 μm-diam device. Other market dominating detectors in same spectral range are plotted for comparison.

Spectral D* of 7 and 10 % Sn photodiodes (measured at 0.1 V reverse bias voltage) is shown in Fig. 53 to directly compare with D* of other market-dominating detectors that use Ge, PbS, InAs, and InGaAs technologies. The spectral response absorption edge is extended to 2.6 μm at 300 K for the 10 % Sn device, which is comparable to the edge-response of an extended-InGaAs detector at 300 K. Compared to our previous study on GeSn photoconductors, the spectral D* here has been improved due to the lower dark current of the present GeSn photodiode. The spectral D* of the 7 % Sn device at 77 K is only one order of magnitude lower than that of extended-InGaAs detectors. A decrease in the device dark current via a thicker GeSn layer and via application of the passivation technique would dramatically reduce the noise. Moreover, a thicker GeSn layer would enhance the absorption in SWIR. Therefore, significantly improved D* of GeSn photodiode detectors can be achieved, making them competitive with commercially available detector technologies in the above-discussed SWIR FPA applications-space.

Publications

Journal

1. Wei Du, Yiyin Zhou, Seyed A. Ghetmiri, Aboozar Mosleh, Benjamin R. Conley, Amjad Nazzal, Richard A. Soref, Greg Sun, John Tolle, Joe Margetis, Hameed A. Naseem, and Shui-Qing Yu, "Room-temperature electroluminescence from Ge/Ge1-xSnx/Ge double heterostructure LEDs on Si substrates via CVD," *Applied Physics Letters* **104**, 241110 (2014)
2. Benjamin R. Conley, Aboozar Mosleh, Seyed Amir Ghetmiri, Wei Du, Richard A. Soref, Greg Sun, Joe Margetis, John Tolle, Hameed A. Naseem, and Shui-Qing Yu, "Temperature dependent spectral response and detectivity of GeSn photoconductors on silicon for short wave infrared detection," *Optics Express* **22**, 15639-15652 (2014)
3. Seyed Amir Ghetmiri, Wei Du, Benjamin R. Conley, Aboozar Mosleh, Amjad Nazzal, Richard A. Soref, Greg Sun, Joe Margetis, John Tolle, Hameed A. Naseem, and Shui-Qing Yu, "Shortwave-infrared photoluminescence from $Ge_{1-x}Sn_x$ thin films on silicon", *Journal of Vacuum Science & Technology B* **32**, 060601 (2014).
4. Wei Du, Seyed A. Ghetmiri, Benjamin R. Conley, Aboozar Mosleh, Amjad Nazzal, Richard A. Soref, Greg Sun, John Tolle, Joe Margetis, Hameed A. Naseem, and Shui-Qing Yu, "Competition of optical transitions between direct and indirect bandgaps in $Ge_{1-x}Sn_x$," *Applied Physics Letters* **105**, 051104 (2014).
5. Seyed Amir Ghetmiri, Wei Du, Joe Margetis, Aboozar Mosleh, Larry Cousar, Benjamin R. Conley, Lucas Domulevicz, Amjad Nazzal, Greg Sun, Richard A. Soref, John Tolle, Baohua Li, Hameed A. Naseem, and Shui-Qing Yu, "Direct-bandgap GeSn grown on Silicon with 2230 nm photoluminescence", *Applied Physics Letters* **105**, 151109 (2014).
6. Benjamin R. Conley, Joe Margetis, Wei Du, Huong Tran, Aboozar Mosleh, Seyed Amir Ghetmiri, John Tolle, Greg Sun, Richard Soref, Baohua Li, Hameed A. Naseem, and Shui-Qing Yu, "Si based GeSn photoconductors with a 1.63A/W peak responsivity and a 2.4μm longwavelength cutoff", *Applied Physics Letters* **105**, 221117 (2014).
7. B. R. Conley, A. Mosleha, S. A. Ghetmiri, W. Du, G. Sun, R. Soref, J. Margetis, J. Tolle, H. A. Naseem, and S.-Q. Yu, "Stability of Pseudomorphic and Compressively Strained $Ge_{1-x}Sn_x$ Thin Films under Rapid Thermal Annealing", *ECS Transactions* **64**, 881-893 (2014).

8. A. Mosleh, M. Alher, L. Cousar, W. Du, S. Ghetmiri, T. Pham, J. Grant, G. Sun, R. Soref, B. Li, H. Naseem and S-Q. Yu, "Direct growth of $Ge_{1-x}Sn_x$ films on Si using a cold-wall ultra-high vacuum chemical-vapor-deposition system", *Frontiers in Materials* **2**, 30 (2015).

9. T. N. Pham, W. Du, B. R. Conley, J. Margetis, G. Sun, R. A. Soref, J. Tolle, B. Li and S. -Q. Yu, "Si based Ge0.9Sn0.1 photo detector with a peak responsivity of 2.85 A/W and a longwave cutoff at 2.4 μm", *Electronics Letters* **51**, 854 (2015). (No acknowledgement included in the paper due to the format requirement)

10. Thach Pham, Wei Du,1, Huong Tran, Joe Margetis, John Tolle, Greg Sun, Richard A. Soref, Hameed A. Naseem, Baohua Li, and Shui-Qing Yu, "Systematic study of Si-based GeSn photodiodes with 2.6 μm detector cutoff for short-wave infrared detection", *Optics Express* **24**, 4519-4531 (2016).

11. Aboozar Mosleh, Murtadha Alher, Larry Cousar, Wei Du, Seyed Ghetmiri, Sattar Al-Kabi, Wei Dou, Perry Grant, Greg Sun, Richard Soref, Baohua Li, Hameed A. Naseem, Shui-Qing Yu, "Buffer-Free GeSn and SiGeSn Growth on Si Substrate Using In Situ SnD_4 Gas Mixing", *Journal of Electronic Materials* **45**, 2051–2058 (2016).

12. Huong Tran, Wei Du, Seyed Ghetmiri, Aboozar Mosleh, Greg Sun, Richard Soref, Joe Margetis, John Tolle, Baohua Li, Hameed A. Naseem, and Shui-Qing Yu, "Systematic study of $Ge_{1-x}Sn_x$ absorption coefficient and refractive index for the device applications of Si-based optoelectronics", *Journal of Applied Physics* **119**, 103106 (2016).

13. Aboozar Mosleh, Murtadha Alher, Wei Du, Larry Cousar, Seyed Ghetmiri, Sattar Al-Kabi, Wei Dou, Perry Grant, Greg Sun, Richard Soref, Baohua Li, Hameed Naseem, and Shui-Qing Yu, "$Si_yGe_{1-x-y}Sn_x$ films grown on Si using a cold-wall ultrahigh-vacuum chemical vapor deposition system", *Journal of Vacuum Science & Technology B* **34**, 011201 (2016).

14. Sattar Al-Kabi, Seyed Ghetmiri, Joe Margetis, Wei Du, Aboozar Mosleh, Murtadha Alher, Wei Dou, Greg Sun, Richard Soref, John Tolle, Baohua Li, Mansour Mortazavi, Hameed A. Naseem, and Shui-Qing Yu, "Optical characterization of Si-based $Ge_{1-x}Sn_x$ alloys with Sn compositions up to 12 %", *Journal of Electronic Materials* **45**, 2133–2141 (2015).

15. A. Mosleh, M. Alher, L. Cousar, H. Abu-safe, W. Dou, P. C. Grant, S. Al-Kabi, S. A. Ghetmiri, B. Alharthi, H. Tran, W. Du, M. Benamara, B. Li, M. Mortazavi, S.-Q. Yu, and H. Naseem, "Enhancement of Material Quality of (Si)GeSn Films Grown By $SnCl_4$ Precursor," *ECS Transactions* **69**, 279-286 (2015).

16. M. Alher, A. Mosleh, L. Cousar, W. Dou, P. C. Grant, S.A. Ghetmiri, S. Al-Kabi, W. Du, M. Benamara, B. Li, M. Mortazavi, S.-Q. Yu, H. A. Naseem, "CMOS Compatible Growth of High Quality Ge, SiGe and SiGeSn for Photonic Device Applications," *ECS Transactions* **69**, 269-278 (2015).

Conference

1. Wei Du, Seyed Amir Ghetmiri, Aboozar Mosleh, Benjamin R. Conley, Liang Huang, Amjad Nazzal, Richard A Soref, Greg Sun, John Tolle, Hameed A. Naseem, and Shui-Qing Yu, "Investigation of Photoluminescence from $Ge_{1-x}Sn_x$: A CMOS-Compatible Material Grown on Si via CVD", *the Conference On Lasers and Electrooptics (CLEO)*, No. JW2A.57, San Jose, CA, USA, June 8-13, (2014).

2. Benjamin R. Conley, Liang Huang, Seyed Amir Ghetmiri, Aboozar Mosleh, Wei Du, Greg Sun, Richard Soref, John Tolle, Hameed A. Naseem, and Shui-Qing Yu, "Extended Infrared Absorption to 2.2 μm with $Ge_{1-x}Sn_x$ Photodetectors Grown on Silicon", *the Conference On Lasers and Electrooptics (CLEO)*, No. SM2H.5, San Jose, CA, USA, June 8-13, (2014).

3. Seyed Amir Ghetmiri, Benjamin R. Conley, Aboozar Mosleh, Liang Huang, Wei Du, Amjad Nazzal, Greg Sun, Richard Soref, John Tolle, Hameed A. Naseem, and Shui-Qing Yu, "Photoluminescence from GeSn/Ge Heterostructure Microdisks with 6% Sn Grown on Si via CVD", *the Conference On Lasers and Electrooptics (CLEO)*, No. AW1H.2, San Jose, CA, USA, June 8-13, (2014).

4. Aboozar Mosleh, Seyed Amir Ghetmiri, Benjamin R. Conley, Wei Du, John Tolle, Shui-Qing Yu,

and Hameed A. Naseem, "Strain Relaxation and Material Quality Improvement of Compressively Strained GeSn Epitaxial Films Through Cyclic Rapid Thermal Annealing Process", *IEEE Summer Topicals Meeting Series*, Montréal, Québec, Canada, July 14-16, (2014).

5. Benjamin R. Conley, Aboozar Mosleh, Seyed A. Ghetmiri, Wei Du, John Tolle, Joe Margetis, Richard A. Soref, Greg Sun, Hameed Naseem, and Shui-Qing Yu, "Temperature Dependent Spectral Response and Responsivity of GeSn Photoconductor on Si", *IEEE Summer Topicals Meeting Series*, Montréal, Québec, Canada, July 14-16, (2014).

6. Wei Du, Seyed Amir Ghetmiri, Aboozar Mosleh, Benjamin R. Conley, Liang Huang, Amjad Nazzal, Richard A. Soref3 Greg Sun, John Tolle, Joe Margetis, Hameed A. Naseem, and Shui-Qing Yu, "Direct transition $Ge_{0.94}Sn_{0.06}$ PIN-diode double heterostructure light emitter at high injection", *the 11th International Conference on Group IV Photonics*, Paris, France, August 27-29, (2014).

7. Benjamin R. Conley, Yiyin Zhou, Aboozar Mosleh, Seyed Amir Ghetmiri, Wei Du, Richard A Soref, Greg Sun, Joe Margetis, John Tolle, Hameed A. Naseem, and Shui-Qing Yu, "Infrared spectral response of a GeSn p-i-n photodiode on Si", *the 11th International Conference on Group IV Photonics*, Paris, France, August 27-29, (2014).

8. Benjamin R. Conley, Aboozar Mosleh, Seyed Amir Ghetmiri, Wei Du, Greg Sun, Richard Soref, John Tolle, Joe Margetis, Hameed A. Naseem, and Shui-Qing Yu, "Stability of pseudomorphic and compressively strained GeSn thin films under rapid thermal annealing", *the 226th ECS Fall Meetings*, Cancun, Mexico, October 5-9, (2014).

9. John Tolle, Joe Margetis, Seyed A. Ghetmiri, Aboozar Mosleh, Benjamin R. Conley, Wei Du, Amjad Nazzal, Richard A. Soref, Greg Sun, Hameed A. Naseem and Shui-Qing Yu, "Growth and characterization of $Ge_{1-x}Sn_x$ alloys deposited using a commercial CVD system", *the 226th ECS Fall Meetings*, Cancun, Mexico, October 5-9, (2014).

10. Yiyin Zhou, Wei Du, Seyed Amir Ghetmiri, Aboozar Mosleh, Amjad Nazzal, Richard A Soref, Greg Sun, Joe Margetis, John Tolle, Hameed A. Naseem, and Shui-Qing Yu, "Room-temperature electroluminescence from $Ge/Ge_{0.92}Sn_{0.08}/Ge$ double heterostructure LED on Si," *IEEE Photonics Conference*, San Diego, CA, USA, October 12-16, (2014). (No acknowledgement included in the paper due to the paper length limit).

11. Thach Pham, Benjamin R. Conley, Liang Huang, Wei Du, Richard A Soref, Greg Sun, Joe Margetis, John Tolle, Hameed A. Naseem, and Shui-Qing Yu, "Enhanced responsivity by integration of interdigitated electrodes on $Ge_{0.93}Sn_{0.07}$ infrared photodetectors," *IEEE Photonics Conference*, San Diego, CA, USA, October 12-16, (2014). (No acknowledgement included in the paper due to the paper length limit).

12. Thach Pham, Benjamin R. Conley, Joe Margetis, Huong Tran, Seyed Amir Ghetmiri, Aboozar Mosleh, Wei Du, Greg Sun, Richard A Soref, John Tolle, Hameed A. Naseem, Baohua Li, and Shui-Qing Yu, "Enhanced responsivity up to 2.85 A/W of Si-based $Ge_{0.9}Sn_{0.1}$ photoconductors by integration of interdigitated electrodes", *the Conference On Lasers and Electrooptics (CLEO) 2015*, STh1I.7, San Jose, CA, USA, May 10~15, (2015). (No acknowledgement included in the paper due to the paper length limit)

13. Seyed Amir Ghetmiri, Wei Du, Yiyin Zhou, Joe Margetis, Thach Pham, Aboozar Mosleh, Benjamin R. Conley, Greg Sun, Richard Soref, John Tolle, Hameed A. Naseem, Baohua Li, Shui-Qing Yu, "Temperature-dependent characterization of $Ge_{0.94}Sn_{0.06}$ Light Emitting Diode grown on Si via CVD", *the Conference On Lasers and Electrooptics (CLEO) 2015*, ATu1J.6, San Jose, CA, USA, May 10~15, (2015). (No acknowledgement included in the paper due to the paper length limit)

14. S.-Q. Yu, S. A. Ghetmiria, W. Du, J. Margetis, Y. Zhou, A. Mosleh, S. Al-Kabi, A. Nazzal, G. Sun, R. A. Soref, J. Tolle, B. Li, H. A. Naseem, "GeSn Photodetector and Light Emitter: Mid-Infrared Devices in Silicon Photonics", **invited talk**, *SPIE Photonic West*, San Francisco, CA, USA, February 7~12, (2015).

15. Thach Pham, Wei Du, Joe Margetis, Seyed Amir Ghetmiri, Aboozar Mosleh, Greg Sun, Richard A Soref, John Tolle, Hameed A. Naseem, Baohua Li, and Shui-Qing Yu, "Temperature-dependent study

of Si-based GeSn photoconductors", *SPIE Photonic West*, San Francisco, CA, USA, February 7~12, (2015).

16. Shui-Qing Yu, Wei Du, Benjamin R. Conley, Seyed A. Ghetmiri, Aboozar Mosleh, Thach Pham, Yiyin Zhou, Amjad Nazzal, Greg Sun, Richard A. Soref, Joe Margetis, John Tolle, and Hameed A. Naseem, "Si based mid-infrared GeSn photo detectors and light emitters on silicon substrates", **invited talk**, accepted by *SPIE Optics + Photonics*, San Diego, CA, USA, August 9~13, (2015).

17. Aboozar Mosleh, Murtadha Alher, Wei Du, Larry C. Cousar, Seyed Amir Ghetmiri, Sattar Al-Kabi, Wei Dou, Perry C. Grant, Benjamin R. Conley, Greg Sun, Richard A. Soref, Baohua Li, Hameed A. Naseem, and Shui-Qing Yu, "Growth and characterization of buffer-free SiGeSn epitaxial layers on Si for photonic applications", *the 57th Electronic Material Conference*, JJ3, Columbus, OH, USA, June 24~26, (2015).

18. Sattar Al-Kabi, Seyed Amir Ghetmiri, Wei Du, Huong Tran, Greg Sun, Richard Soref, John Tolle, Joe Margetis, Baohua Li, Hameed A. Naseem, and Shui-Qing Yu, "Material and Optical Characterizations for Both Bulk and NIP Double Heterostructure of Germanium Tin", *the 57th Electronic Material Conference*, PS4, Columbus, OH, USA, June 24~26, (2015).

19. Wei Du, Seyed A. Ghetmiri, Yiyin Zhou, Aboozar Mosleh, Joe Margetis, John Tolle, Greg Sun, Richard A. Soref, Baohua Li, Hameed Naseem, and Shui-Qing Yu, "Si-Based GeSn Edge-Emitting LEDs with Sn Compositions up to 8%", **invited talk**, *2015 IEEE Summer Topicals*, Nassau, Bahamas, July 13-15, (2015).

20. A. Mosleh, M. Alher, L. Cousar, H. Abu-safe, W. Dou, P. C. Grant, S. Al- Kabi,, S.A. Ghetmiri, B. Alharthi, H. Tran, W. Du, M. Benamara, B. Li ,M. Mortazavi, S.-Q. Yu, and H. Naseem, "Enhancement of Material Quality of (Si)GeSn Films Grown By $SnCl_4$ Precursor", *2015 ECS fall (228th meeting)*, October 11-16, Phoenix, AZ (2015).

21. M. Alher, A.Mosleh, L. Cousar, W. Dou, P. C. Grant, S.A. Ghetmiri, S. Al-Kabi, W. Du, M. Benamara, B. Li, M. Mortazavi, S.-Q. Yu, and H. A. Naseem, "CMOS Compatible Growth of High Quality Ge, SiGe and SiGeSn for Photonic Device Applications", *2015 ECS fall (228th meeting)*, October 11-16, Phoenix, AZ (2015).

22. Thach Pham, Wei Du, Huong Tran, Joe Margetis, John Tolle, Greg Sun, Richard Soref, Hameed Naseem, Baohua Li, Mansour Mortazavi, and Shui-Qing Yu, "Systematic study of Si-based $Ge/Ge_{0.9}Sn_{0.1}/Ge$ photodiodes with 2.6 μm detector cutoff", *the Conference On Lasers and Electrooptics (CLEO)*, No. STh1G.7, San Jose, CA, USA, June 5-10 (2016).

23. Joe Margetis, John Tolle, Wei Du, Aboozar Mosleh, Sayed A. Ghetmiri, Hameed Naseem, and Shui-Qing Yu, "$Ge_{1-x}Sn_x$ and $Si_yGe_{1-x-y}Sn_x$ epitaxy on a commercial CVD reactor", ***invited talk***, *IEEE Summer Topicals Meetings*, Newport Beach, CA, USA, July 11-13 (2016).

24. Huong Tran, Thach Pham, Yiyin Zhou, Seyed Ghetmiri, Sattar Al-Kabi, Aboozar Mosleh, Hameed Naseem, Shui-Qing Yu, John Tolle, Joe Margetis, Wei Du, Mansour Mortazavi, Richard Soref, Greg Sun, and Baohua Li, "Investigation of Si-based $Ge_{0.93}Sn_{0.07}$ Photoconductors towards Short-wave Infrared Detection", *IEEE Summer Topicals Meetings*, Newport Beach, CA, USA, July 11-13 (2016).

Provisional patents

1. Aboozar Mosleh, Larry C. Cousar, Murtadha A. Alher, Shui-Qing Yu, Hameed A. Naseem, "Heteroepitaxial Growth of Ge-Sn Alloys", application No.: 62097914 (2014).

2. Benjamin Ryan Conley, Shui-Qing Yu, Richard Soref, "Systems and Methods for Digital Night Vision", application No.: 62150119 (2015).